

Article

Apatite Chemical Compositions from Acadian-Related Granitoids of New Brunswick, Canada: Implications for Petrogenesis and Metallogenesis

Zeinab Azadbakht , David R. Lentz  and Christopher R.M. McFarlane

Department of Earth Sciences, University of New Brunswick, P.O. Box 4400, Fredericton, NB E3B 5A3, Canada; dlentz@unb.ca (D.R.L.); crmm@unb.ca (C.R.M.M.)

* Correspondence: Zeinab.azadbakht@unb.ca; Tel.: +1-639-316-4080

Received: 31 October 2018; Accepted: 12 December 2018; Published: 17 December 2018



Abstract: The geochemistry of apatite crystals from fifteen fertile and infertile Acadian-related granitoids of New Brunswick (Canada) was studied *in situ*, using electron microprobe and laser ablation-inductively coupled plasma-mass spectrometry to further investigate petrogenesis and fertility index among these intrusions. The results indicate a clear geochemical contrast between barren and mineralized samples where apatite grains from barren intrusions are the most hydrous (OH > 0.3 wt. %), with lowest Mn (<1700 ppm), Fe (<800 ppm), and Sn (<0.01 ppm). In contrast, apatite grains from Cu-Mo related intrusions are distinguished by higher Cl (>0.1 wt. %), (La/Yb)_N ratios of 21.17, (Eu/Eu*)_N ratios of 0.30, and LREE/HREE ratios of 6.03. Apatites from Sn-W related magmatic suites have the highest F (>3 wt. %), Mn (>5350 ppm), Fe (>2200 ppm), Y (>4900 ppm), Sn (>2 ppm), and the lowest Cl (<0.01 wt. %), Sr (<60 ppm), U (<18 ppm), Th (<29 ppm), (Eu/Eu*)_N ratios (<0.01), and (La/Yb)_N ratios (<0.88). Lastly, apatite grains from Mo-bearing systems have the lowest SiO₂ (<0.4 wt. %), Sr (<33 ppm), Th (<28 ppm), a moderate Mn (~3800 ppm), Y (~3500 ppm), and highest FeO_t (<0.9 wt. %). However, the results indicated apatite Mn, Sr, LREE/HREE, and (Eu/Eu*)_N ratios as the best fertility indices used for discriminating barren from fertile granite intrusions.

Keywords: apatite; trace element composition; granite; New Brunswick; Appalachian

1. Introduction

Apatite, Ca₅(PO₄)₃(F, Cl, OH), is one of the most common accessory minerals and the most abundant phosphate phase in most igneous rocks (Piccoli and Candela [1]). Its composition depends mainly on the composition of the host melts, temperature, and oxygen fugacity (Pan and Fleet [2], Marks et al. [3]). Despite appearing as an accessory phase, apatite chemistry plays a significant role in documenting the history of magmatic evolution of magmas. In fact, the crystallization of phosphate phases, especially apatite, is an important process in magmatic systems as the residence of U, Th, Sr, and REE is controlled through melt/phosphate mineral equilibria (Hughes et al. [4], Toplis and Dingwell [5]). Furthermore, apatite can preserve information about magmatic and post-magmatic processes due to its early formation and long stability during the differentiation of magmatic systems (Lisowiec et al. [6]). Many elements can substitute within apatite crystal structure, making this mineral a proxy for thermochronological studies, radiometric, and fission track dating (Nemchin and Pidgeon [7], Chamberlain and Bowring [8], Gleadow et al. [9], Harrison et al. [10], Carrapa et al. [11], Chew et al. [12], Tang et al. [13], Vamvaka et al., [14]), determination of oxygen fugacity (Cao et al. [15], Miles et al. [16], Marks et al. [3]), determination of halogen fugacity (Zhu and Sverjensky [17], Teiber et al. [18]), thermometry (Stormer and Carmichael [19], Ludington [20], Wones [21], Munoz [22],

Zhu and Sverjensk [17], Sallet [23]), and the study of magma evolution history (Ishihara [24], Nash [25], Teiber et al. [26], Ishihara and Moriyama [27]). Furthermore, apatite geochemical characteristics can be used to study granitoid petrogenesis (Sha and Chappell [28], Chu et al. [29], Cao et al. [15], Ding et al. [30]) and secondary metasomatic processes (Zirner et al. [31], Broom-Fendley et al. [32]). More importantly, apatite trace element composition can also be used as a mineral exploration tool (e.g., Roegge et al. [33], Williams and Cesborn [34], Belousova et al. [35,36], Imai [37,38], Cao et al. [15], Boswell [39], Mao et al. [40], Duan and Jiang [41]).

Felsic intrusions in New Brunswick are commonly associated with different styles of granophile element mineralization including porphyry, skarn, greisen, and vein-related deposits. However, some of the intrusions are barren despite their highly fractionated nature (Whalen [42]). This motivated the authors to investigate apatite geochemical characteristics including major and trace elements, along with the halogen content from fifteen of these Late Silurian to Late Devonian intrusions formed in the Acadian orogeny to investigate the petrogenesis of these granitoids and to examine the application of detailed apatite compositions as a proxy to differentiate between barren and mineralized granitoids of New Brunswick (Figure 1).

2. Geological Setting

Fifteen felsic intrusions of Late Silurian to Late Devonian age in New Brunswick were selected for this study; these intrusions vary in composition from granodiorite to granite and are mostly (except Blue Mountain Granite and Nicholas Dénys Granodiorite) located within the Central plutonic belt of New Brunswick (Table 1). The plutonic belt extends from Chaleur Bay in northeastern New Brunswick and extends toward the southwest of the province passing the American border into adjacent Maine (Azadbakht et al. [43]). The belt encloses many calc-alkaline, non-foliated and foliated Silurian-Devonian felsic intrusions, which intrude the Cambrian to Early Ordovician rocks of the Woodstock, Miramichi, and Meductic groups, Bathurst Supergroup, and the Trousers Lake metasedimentary Suite (Wilson and Kamo [44]). The plutonic belt cuts three out of four (excluding Humber zone) lower Paleozoic tectonomagmatic zones including Dunnage, Gander, and Avalon from northwest to southeast. The Humber Zone stretches across the Gaspésie, Quebec and northern New Brunswick and represents the western margin of the Iapetus Ocean, which was deposited over the Grenville lower crustal block (Whalen [42], Whalen et al. [45]). The Dunnage Zone occurs in northern New Brunswick and is comprised of the allochthonous remnants of Iapetus ocean floor, arc and back-arc sequences and is underlined by the Grenville basement in the western part and by the Central lower crustal block in the eastern part (Whalen [42], Whalen et al. [45]). The Gander Zone occurs in most of New Brunswick and represents the eastern continental margin of the Iapetus Ocean.

Table 1. Summary of sample localities, ages, associated mineralization, and accessory phases of granitoids in New Brunswick. Mineral abbreviations are after Whitney and Evans [46].

#	Sample	Locality	Lithology	Age (Ma)	Associated Mineralization	Other Halogen Bearing Minerals	Accessory Mineral Phase
1	WX85NB-47	Nicholas Dénys	Bt granodiorite	381 ± 4 ¹	Porphyry Cu-Mo	Bt, Amp	Mag, Ilm, Zrn, Ttn, Ep
2	WX85NB-46	Pabineau Falls	Alf porphyry Bt granite	397.2 ± 1.9 ²	Vein Mo	Bt, Amp	Zrn, Mnz, Xtm, Ilm
3	WX86NB-254	Mt LaTour	Bt granite	417.7 ± 4.4 ³	Barren	Bt,	Zrn, Mnz
4	DS06-0077-2	Long Lake	Ms leucogranite	406.1 ± 1.9 ⁴	Vein U-Mo	Bt, Chl, Ms	Zrn, Mnz, Ilm
5	WX85NB-226	Dungarvon	Qz porphyry Bt granite	376 ± 4 ⁵	Vein Sn-W	Bt	Zrn, Ilm
6	WX85NB-225	Trout Lake	Qz porphyry Bt granite	380.6 ± 0.3 ⁶	Vein Sn-W	Bt	Zrn, Ilm, Mnz, Ep, Xtm
7	WX85NB-161	Lost Lake	Bt-Ms granodiorite	409.7 ± 0.5 ⁶	Barren	Bt, Ms	Ilm, Ttn, Zrn
8	WX85NB-11	Hawkshaw	Afs porphyry Bt granite	411 ± 1 ⁷	Vein Cu-Au-W	Chl	Mag, Ilm, Zrn, Rt
9	WX85NB-38	Allandale	Bt-Ms granite	402 ± 1 ⁸	Vein Be-Mo	Bt	Zrn, Ilm, Ep, Mnz, Ttn
10	LG	Lake George	Granodiorite	412 ± 2 ⁹	Barren	Bt, Chl, Amp	Zrn, Mnz, Cal, Ep
11	2010-CB-16B	Evandale	Granodiorite	390.4 ± 1.5 ¹⁰	Porphyry Cu-Mo	Bt, Amp	Mag, Zrn, Ilm, Ep, Rt
12	WX85NB-196	Magaguadavic	Afs porphyry Bt-Amp granite	403 ± 2 ¹¹	Vein Cu-Mo	Bt	Zrn, Ttn, Ilm, Mag, Aln
13	WX85NB-198 WX85NB-220	Mount Douglas	Bt granite-Dmd ₁	366 ¹²	Barren	Bt, Fl Bt, Chl, Fl	Mag, Ilm Mag, Zrn, Ilm
14	WX85NB-188	Beech Hill	Fsp-Qz-Bt porphyry granite	343 ± 33 ¹³	Vein Sn-W	Bt, Chl	Zrn, Ilm
15	WX85NB-189	Utopia	Bt granite	428.3 ± 1.0 ¹¹	Vein Mo-Sn	Bt	Zrn, Ilm, Mag, Mnz, Aln

¹ Walker et al. [47]; ² Whalen [42]; ³ Azadbakht et al. [43]; ⁴ Shinkle [48]; ⁵ MacLellan et al. [49]; ⁶ Wilson and Kamo [44]; ⁷ Bevier and Whalen [50]; ⁸ Beal et al. [51]; ⁹ Yang et al. [52]; ¹⁰ White [53]; ¹¹ Mohammadi et al. [54]; ¹² McLeod [55]; ¹³ Yang [56].

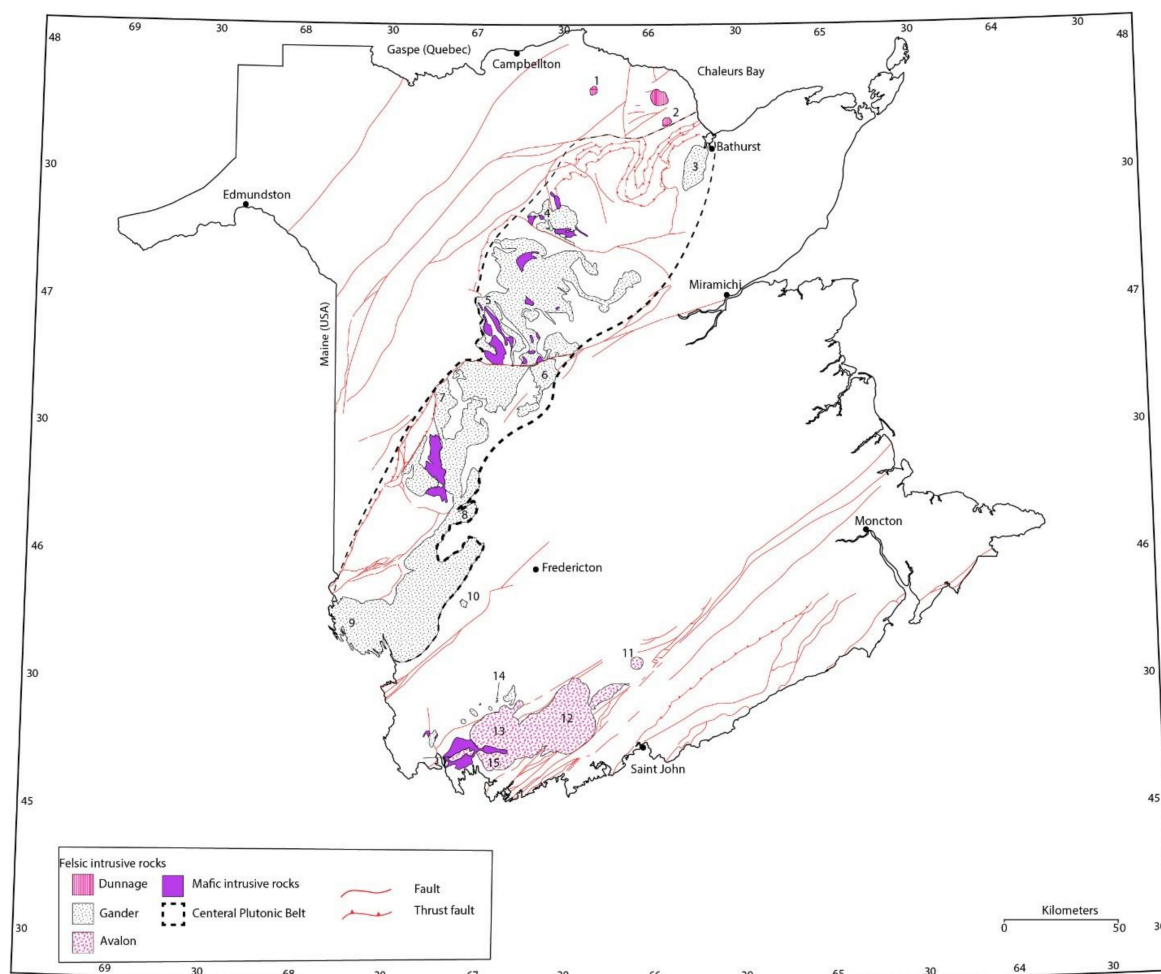


Figure 1. Lithological map of New Brunswick (Canada) modified after Fyffe and Richard [55] showing the location of the studied granitoid intrusions. 1—Blue Mountain Granite, 2—Nicholas Dénys Granodiorite, 3—Pabineau Falls Granite, 4—Mount LaTour Granite, 5—Long Lake Granite, 6—Dungarvon Pluton, 7—Lost Lake Granite, 8—Hawkshaw Granite, 9—Allandale Granite, 10—Lake George Granodiorite, 11—Evandale Granodiorite, 12—Mount Douglas Granite, 13—Magaguadavic Granite, 14—Beech Hill Granite, 15—Utopia Granite.

These tectonomagmatic zones are underlain by the Central lower crustal block (Whalen [42], Whalen et al. [56,57]). Finally, the Avalon Zone occurs in southwestern New Brunswick and indicates a stable platform in the early Paleozoic. Avalonia was accreted on the Avalon lower crustal block (Whalen [42], Whalen et al. [58], Whalen et al. [56]). The accretion and deformation of these tectonomagmatic zones during different stages of the Appalachian orogenic cycle is represented by a series of orogenic events including Taconic, Salinic, Acadian, and Neo-Acadian spanning Ordovician to Early Carboniferous time, respectively (van Staal et al. [59]). These rocks were then subsequently covered by the Late Devonian to early Permian Maritimes successor basin (Yang et al. [60]).

3. Studied Mineral Deposits and Their Host Rocks

Two series of felsic intrusions were emplaced during the later stages of the Appalachian orogenic cycle in New Brunswick. These intrusions show a variety of geochemical characteristics from primitive to highly evolved A-, S-, and I-types granitoids (see Whalen [42]). Those associated with crustal thickening processes of the Acadian orogeny and post-Acadian uplift are locally mineralized with granophile elements. Fifteen of these Late Silurian to Late Devonian intrusions (Figure 1) with diverse characteristics were selected to investigate detailed apatite compositions (major elements,

halogens, and trace elements geochemical composition) to test whether apatite can be used as a mineral exploration tool to distinguish between barren and mineralized Acadian-related granitoids. The following descriptions of the intrusions are taken from the Lexicon of NB geology as posted on the website of New Brunswick Department of Energy and Resource Development [61]. Associated mineral occurrences (Unique Reference Number-URN) are cited from the New Brunswick Department of Energy and Resource Development computerized database [62]. The depth of emplacement of the plutons are not precisely known as there are few available Al in hornblende data for the examined intrusions. However, the presence of porphyritic texture, miarolitic cavities, and pegmatitic dikes associated with many of the intrusions, points to the high level of emplacement (1.5–2.5 km). To further investigate the depth of emplacement, the pressure of crystallization was calculated following the method of Yang [63] where the pressure varies between 0.5 to 5.3 kbar among the studied intrusions.

3.1. Barren Intrusions

3.1.1. Mount LaTour Granite

This Early Devonian (U-Pb monazite age of 417.7 ± 4.4 Ma; Azadbakht et al. [43]), heterogeneous granitic intrusion forms the western portion of the South Nepisiguit River Plutonic Suite in northeastern New Brunswick. It comprises five phases, and the most abundant phase (WX85NB-254) is an amphibole-bearing medium- to coarse-grained, equigranular alkaline granite, which contains only alkali-feldspar (i.e., hypersolvus granite). The sample is a coarse-grained equigranular white biotite granite with A/CNK ($\text{Al}_2\text{O}_3/(\text{CaO} + \text{Na}_2\text{O} + \text{K}_2\text{O})$) of 1.01 and A/NK ($\text{Al}_2\text{O}_3/(\text{Na}_2\text{O} + \text{K}_2\text{O})$) of 1.16 identifying the sample as a peraluminous I-type granite. In general, the sample is altered and most of the amphibole and mica grains are replaced by secondary minerals.

3.1.2. Lost Lake Granite

This Early Devonian heterogeneous granitic body (U-Pb zircon age of 409.7 ± 0.5 Ma; Wilson and Kamo [44]) covers an area of 120 km² in central New Brunswick. It is composed mainly of medium-grained equigranular biotite-muscovite granite (WX85NB-161), with minor muscovite granite and pegmatite in southern portion (Whalen [42]; Whalen et al. [57]). The pegmatitic pods in this granite are related to minor Be mineralization (URN 295). The sample is a coarse-grained equigranular biotite-muscovite granite with A/CNK of 1.06 and A/NK of 1.63 identifying the sample as a weakly peraluminous I-type granite. In general, all the phenocrysts show signs of deformation like undulose extinction in quartz and curved cleavage lines in both biotite and muscovite.

3.1.3. Mount Douglas Granite

This heterogeneous granite forms the eastern portion of the Saint George Batholith (SGB) in southwestern New Brunswick and underlies an area of 600 km² (Whalen et al. [56]). An agreement between ca. 367 Ma ⁴⁰Ar-³⁹Ar biotite age reported by McLeod et al. [64] and U-Pb zircon age (367 ± 1 Ma; Bevier [65]) identified this intrusion as the youngest phase of the SGB. McLeod [66] divided this intrusion into three sequentially emplaced phases from a coarse-grained seriate, biotite, hornblende granite of Dmd₁ (WX85NB-198 and 220) to pink medium- to fine-grained, seriate, biotite granite of Dmd₂, and red, medium-grained, equigranular, biotite granite of Dmd₃. The first phase (Dmd₁) is barren; however, the other two phases are associated with significant endogranite Sn, W, Ag, Mo, As, Bi, Cu, Pb, and Zn-bearing veins, as well as, wall rock alteration in more than thirty localities including URNs 18, 218, 225 to 330 containing 0.2% Sn, 123 g/t Ag, 1.89 g/t Au, 0.36% Cu, and 8.32% Zn. The samples are white-pink medium- to coarse-grained seriate biotite granite with rapakivi feldspars, large (greater than 1mm) brown biotite crystals, ACNK of 0.97, and A/NK of 1.13 identifying them as a metaluminous I-type granite.

3.2. Fertile Intrusions Associated with Cu-Mo Mineralization

3.2.1. Hawkshaw Granite

This Early Devonian granite (U-Pb titanite age of 411 ± 1 Ma; Bevier and Whalen [50], Whalen et al. [57]) underlies an area of about 700 km² and forms most of the eastern half of the Pokiok Batholith in southwestern New Brunswick (Figure 1). It is composed of a coarse-grained porphyritic biotite granite (WX85NB-11) to granodiorite with minor equigranular biotite granite (Whalen [42]). This intrusion is related to minor greisen and stockwork vein Sn mineralization (URN 530), veins of purple fluorite (RF 534), and significant quartz-carbonate veins containing Cu, Au, and W (URN 657) with up to 0.52% W. The sample is a medium-grained pink potassium feldspar porphyry biotite granite with ACNK of 0.99 and A/NK of 1.38 identifying it as a metaluminous I-type granite.

3.2.2. Nicholas Dénys Granodiorite

This middle Devonian (U-Pb zircon age of 381 ± 4 Ma; Walker et al. [47], Whalen et al. [45]) medium-grained, equigranular, biotite granodiorite (WX85NB-47) underlies an area of 12 km² in northeastern New Brunswick. The Nicholas Dénys granodiorite is associated with quartz veinings, stockworks, and disseminated base metal (commonly Cu, Fe) mineralization along its contact aureole with the highly fractured Silurian Chaleur Group, containing 0.11 g/t Ag, 156 ppm Cu, and 107 ppm Mo (URNs 47, 440, and 1063). The sample is a medium-grained equigranular biotite granodiorite with A/CNK of 0.96 and A/NK of 1.46 identifying it as a metaluminous I-type granite. The sample shows signs of secondary alteration with many of the minerals displaying resorbed boundaries.

3.2.3. Evandale Granodiorite

This circular stock is a heterogeneous Middle Devonian (U-Pb zircon age of 390.4 ± 1.5 Ma; White [53]) granodiorite (2010-CB-16B), which covers an area of about 20 km². It is composed of a medium-grained equigranular hornblende-biotite granodiorite to monzogranite, which is cut by minor narrow, north-northwest-trending aplite dikes (White [53]). This intrusion has characteristics of a porphyry deposit, and its aplitic dikes are related to disseminated Cu, Au, Ag mineralization with 322 g/t Ag, 16.1 g/t Au, 2.4% Cu, 4.7% Pb, and 6.7% Zn (URN 11). Further study by White [53] proposed the possibility of more enriched portions of the intrusion at depth or the erosion of mineralized zone. The sample is a coarse-grained amphibole-bearing granodiorite with A/CNK of 1.13 and A/NK of 1.24 identifying it as a peraluminous granodiorite.

3.2.4. Magaguadavic Granite

This Early Devonian multiphase granite (U-Pb zircon age of 396 ± 1 Ma by Bevier and Barr [67], 403 ± 2 Ma by Mohammadi et al. [54]) is a large pluton (21 km × 15 km), which forms the western to central portion of the Saint George Batholith in southwestern New Brunswick (McLeod [66]). Pegmatitic to aplitic felsic dikes of this intrusion are associated with disseminated Au mineralization containing up to 6.33 g/t Au (URN 1405) (Thorne et al. [68]). This granite (WX85NB-196) is also related to hornfels Mo, Cu mineralization of Spring Brook and Clarence Brook occurrences with 0.25% Mo (URN 347 and 775). The sample is a very coarse-grained potassium feldspar porphyry biotite granite with rapakivi feldspar and large biotite crystals (greater than 1mm). It has A/CNK of 0.95 and A/NK of 1.30 identifying the intrusion as metaluminous I-type granite.

3.3. Fertile Intrusions Associated with Mo Deposits

3.3.1. Pabineau Falls Granite

This Middle Devonian coarse-grained equigranular to sub-porphyritic biotite granite (WX85NB-46); U-Pb zircon age of 397.2 ± 1.9 Ma; Whalen [42]) underlies an area of 150 km² in northern New Brunswick (Whalen et al. [57]). This intrusion is related to both minor and significant

endogranitic disseminated and aplitic dikes associated Mo, Be mineralization containing 5.02% Mo (URN 65,123, 133, and 1314). It is also related to minor gold-bearing quartz veins containing 0.69 g/t Au (URN 166). The sample is a coarse-grained potassium feldspar porphyry biotite granite with A/CNK of 1.03 and A/NK of 1.30 identifying it as a weakly peraluminous I-type granite.

3.3.2. Long Lake Leucogranite

The Long Lake occurrence is associated with high level, highly fractionated phases of the Devonian North Pole Stream Granitic Suite. Long Lake granite is a U-rich strongly peraluminous, slightly perphosphoric, muscovite leucogranite dike (DS06-0077-2), which crosscuts the North Pole Stream Granite (NPSG) at the Long Lake area (Shinkle [48]). The 11-million-year time difference from the emplacement of the North Pole intrusive complex ($^{40}\text{Ar}/^{39}\text{Ar}$ muscovite age of 406.1 ± 1.9 Ma; Shinkle [48]) indicates that the dikes must have been emplaced during the latest stages of the Acadian Orogeny. This dike is associated with disseminated U-Mo mineralization (URN 64) containing 20.04% Mo and 0.4% UO_2 and U-Mn mineralization (URN 1274) containing 0.58% UO_2 . The sample is a medium-grained biotite granite with A/CNK of 1.53 and A/NK of 1.73 identifying it as a highly peraluminous S-type granite. The sample show signs of secondary alteration with most of the biotites replaced by chlorite.

3.3.3. Allandale Granite

This granite represents the youngest (U-Pb monazite age of 402 ± 1 Ma; Bevier and Whalen [50]; Whalen et al. [56]) and the most evolved phase of the Pokiok Batholith (PKB), which intrudes the Hawkshaw Granite. Allandale Granite (WX85NB-38) is primarily a fine- to medium-grained equigranular muscovite-biotite granite, which underlies an area of 375 km². This intrusion is related to pegmatite-aplite dikes and vein-type Be and Mo mineralization at Zealand Station with 6.8 g/t Au and 0.74% BeO (RN 219) and Au mineralization with 6.8 g/t Au at the Zealand Au occurrence (RN 902) (Beal et al. [51]). The sample is a medium- to coarse-grained seriate biotite-muscovite granite with A/CNK of 1.03 and A/NK of 1.30 identifying it as a weakly peraluminous I-type granite.

3.3.4. Utopia Granite

This homogenous Late Silurian (U-Pb monazite age of 425.5 ± 2.1 Ma; Mohammadi et al. [54]) intrusion forms the southwestern part of the Saint George Batholith and covers an area of about 90 km² (McLeod [66]). The Utopia Granite (WX85NB-189) consists mainly of medium- to coarse-grained, light to dark red transition syenogranite to monzogranite. This intrusion is related to minor disseminated mineralization of Sn, Mo, and Cu (URN 595), U mineralization with 0.01% U_3O_8 (URN 700), greisen F-Sn mineralization with 0.96% F and 0.01% Sn (URN 816), and significant disseminated, vein filling F, Mo, Sn, and Ag mineralization containing 0.83% Mo (URN 596). The sample is a medium- to coarse-grained equigranular pink biotite granite with A/CNK of 1.00 and A/NK of 1.13 identifying it as a metaluminous I-type granite.

3.4. Fertile Intrusions Associated with Sn-W Deposits

3.4.1. Dungarvon Pluton

This Middle Devonian ($^{40}\text{Ar}/^{39}\text{Ar}$ muscovite age of 376 ± 4 Ma; MacLellan et al. [49]) composite pluton comprises the eastern part of the Burnthill Granites in central New Brunswick. It covers an area of about 140 km² (MacLellan et al. [49], Whalen et al. [57]). It is composed mainly of an equigranular to porphyritic biotite microgranite (WX85NB-225 and 226) with minor pegmatite, aplite, and granophyric granite, and a medium- to coarse-grained equigranular to porphyritic biotite granite (MacLellan et al. [49], Smith and Fyffe [69]). This intrusion is related to significant vein mineralization of Sn, W, F, Mo, Cu, Ag, Mn, Zn at several localities containing 0.67% Sn, 0.43% Mo, 5.35% W, 17.5 g/t Ag, 2% Zn, 14.4% Mn (URN 298, 300, 302 510, 511, 512, 1191, 1169). It is also associated with minor

vein related U anomaly (URN 297) and disseminated Cu mineralization (URN 303, 1170). The samples are medium-grained pink feldspar-quartz porphyry biotite granite with A/CNK of 1.00 and A/NK of 1.20 identifying them as metaluminous I-type granite.

3.4.2. Beech Hill Granite

This granite is a circular porphyritic biotite granite (WX85NB-188), which covers an area of about 8 km² (Whalen et al. [56]). Yang et al. [60] recalculated the Butt [70] data and indicated a Rb-Sr whole rock age of 343 ± 33 Ma with an initial ⁸⁷Sr-⁸⁶Sr ratio of 0.712 ± 0.020 (MSWD = 4.4). These authors consider that the age does not reflect the emplacement or the mineralization age. Mineralized fractures and veinlets in both sedimentary rocks and the greisenized granite are associated with Sn, F, Zn, and Mo mineralization containing 0.17% Mo, 0.13% Sn, and 0.77% WO₃ (RN 683, 684). The sample is a fine-grained beige feldspar-quartz-biotite porphyry granite with A/CNK of 0.96 and A/NK of 1.09 identifying it as a metaluminous I-type granite. The sample is highly altered.

3.4.3. Lake George Granodiorite

This Early Devonian (U-Pb zircon age of 412 ± 2 Ma; Yang et al. [52]) granodiorite (LG) is related to the Hawkshaw Granite, a phase of the Pokiok Batholith produced through fractional crystallization (Yang et al. [71,72]). The Lake George granodiorite stock is considered the source for heat and water for early hydrothermal W-Mo-Au and later Au-Sb mineralization containing up to 11.7 g/t Au and 3.45% Sb (URNs 6, 7, and 1280) (Yang et al. [52]) associated with the granodiorite. Samples vary from fine- to medium-grained white biotite granite to granodiorite with A/CNK of 0.98 to 1.04 and A/NK 1.53 to 1.82 identifying them as metaluminous to peraluminous I-type granitoids. Most of the samples are highly altered and biotite is completely replaced by either chlorite or muscovite.

4. Materials and Analytical Techniques

A detailed petrographic study of representative granitoid samples identified textural relations of apatite to other rock-forming minerals that allowed us to select those apatite crystals free of mineral inclusions for chemical analysis. Major, minor element, and halogen compositions of apatite were determined *in situ* on carbon-coated polished thin sections using a JXA JEOL-733 electron microprobe analyzer (EPMA) (JEOL, Ltd., Akishima, Japan), equipped with dQuant32 and dSpec automation from Geller Microanalytical Laboratories at the University of New Brunswick. The wavelength dispersive spectroscopy (WDS) operating conditions were 15 kV accelerating voltage, 30 nA beam current, and a maximum of 200s counting for Ce. The Wilberforce Apatite was used as the standard, and the accuracy of the data is better than 2% for all the elements. Detection limit is 0.02, 0.03, 0.01, and 0.01 wt. % for Cl, F, Ba, and S. Formula calculation for apatite is based on 25 oxygen. $OH = 1.79 (1 - F/3.767) - (Cl/6.809)$ and $O=F, Cl = (F \times (16/70.9)) + (Cl \times (16/38))$ where F and Cl are in wt. % (Piccoli and Candela [68]). Mole fractions of fluorapatite (FAp), chlorapatite (ClAp), and hydroxyapatite (HAp) were calculated following the equations presented in Piccoli and Candela [1].

Cathodoluminescence (CL) emission of the apatite crystals was collected using a Jeol-JSM-6400 Scanning electron microscope (SEM) (JEOL, Ltd., Akishima, Japan) equipped with a Gatan ChromaCL Cathodoluminescence imaging system at the University of New Brunswick. The accelerating voltage was 15 kV, with a probe current of approximately 11 nA, and using a dwell time of 200 μs per pixel.

The studied apatite grains were then analyzed for trace elements including rare earth elements (REEs) by a laser ablation-inductivity coupled plasma-mass spectrometer (LA-ICP-MS) using a Resonetics RESolution Series M-50-LR 193 nm ArF Excimer laser ablation system (Resonetics, Nashua, NH, USA) coupled to an Agilent 7700× quadrupole ICP-MS (Agilent Technologies, Santa Clara, CA, USA) at the University of New Brunswick. The Ca content of each spot as measured by EPMA was used as the internal standard, with an internally standardized data reduction scheme to obtain the most accurate trace element data. The NIST SRM 610 glass was used for external calibration, whereas the NIST SRM 612 glass was analyzed as a quality control check in runs [73]. Standards

and unknowns were ablated with 33 μm diameter craters using a repetition rate of 4 Hz, and 140 mJ energy. Typical ablation time was 35 s, with 35 s background collection. Zoned apatite crystals were analyzed along a 5 μm -sized crater raster line, oriented perpendicular to the observed zoning feature, from rim to rim. Collected data agree with the recommended values of the standards with precision better than 5% for most of the 20 elements. It is noted that apatite grains from several of the intrusions including Lake George, Nicholas Dénys, and Evandale granodiorites, Allandale, Long Lake, and Papineau Falls granites are beam sensitive in a way that all the grains were extensively damaged (pitted out) or destroyed by either of the EPMA or LA-ICP-MS beams. As a result, a complete data set is not available for all the investigated apatite grains from these intrusions. Representative chemical compositions of the apatites are shown in Table 2. Whole rock SiO_2 content is cited and tabulated in Whalen [42].

Table 2. Mean major- and trace-element composition of apatites from Acadian-related granitoids of New Brunswick.

Sample	WX85NB-254	WX85NB-198	WX85NB-220	WX85NB-161	WX85NB-47	WX85NB-196	2010-CB-16						
Intrusion	Mount LaTour	Mount Douglas (Dmd1)		Lost Lake	Nicholas Dénys	Magaguadavic	Evandale						
Mineralization	Barren	Barren		Barren	Cu-Mo	Cu-Mo	Cu-Mo						
No of Grains	1	9	6	3	2	2	2						
Major elements (wt. %)		Av.	1σ	Av.	1σ	Av.	1σ	Av.	1σ	Av.	1σ	Av.	1σ
P ₂ O ₅	41.05	40.10	0.8	39.71	1.3	41.40	0.9	37.66	5.1	40.50	0.7	40.46	0.1
CaO	53.86	54.05	1.1	53.32	1.6	54.82	0.0	49.37	7.9	54.30	0.3	53.88	0.0
SiO ₂	0.32	0.83	0.5	0.75	0.5	0.40	0.2	2.69	3.4	0.56	0.2	0.35	0.1
FeO	0.52	0.60	0.3	0.65	0.1	0.23	0.1	1.58	1.5	0.25	0.1	0.36	0.0
MnO	0.12	0.08	0.0	0.21	0.0	0.21	0.1	0.15	0.0	0.10	0.0	0.08	0.0
SrO	0.00	0.00	0.0	0.00	0.0	0.00	0.0	0.00	0.0	0.02	0.0	0.02	0.0
Y ₂ O ₃	0.38	0.25	0.2	0.85	0.6	0.13	0.0	0.26	0.1	0.00	0.0	0.00	0.0
Ce ₂ O ₃	0.30	0.64	0.4	0.68	0.3	0.13	0.0	0.14	0.1	0.58	0.0	0.38	0.1
UO ₂	0.04	0.01	0.0	0.00	0.0	0.10	0.1	0.00	0.0	0.00	0.0	0.22	0.2
BaO	0.00	0.00	0.0	0.00	0.0	0.00	0.0	0.09	0.1	0.00	0.0	0.00	0.0
Cl	0.11	0.01	0.0	0.02	0.0	0.01	0.0	0.24	0.0	0.04	0.0	0.29	0.0
F	3.38	3.08	0.4	3.40	0.2	3.13	0.1	2.82	1.4	3.00	0.0	2.81	0.3
SO ₃	0.00	0.05	0.1	0.02	0.0	0.01	0.0	0.09	0.1	0.14	0.0	0.14	0.0
O=F,Cl	1.45	1.30	0.2	1.44	0.1	1.32	0.0	1.24	0.6	1.27	0.0	1.25	0.1
Total	98.63	98.40	-	98.17	-	99.25	-	93.85	-	98.23	-	97.72	-
Trace elements (ppm)													
Sr	36	74	31	27	9	93	3	-	-	120	34	-	-
Th	15	289	145	93	26	23	13	-	-	108	49	-	-
U	13	62	30	24	9	264	97	-	-	26	12	-	-
La	883	3411	1228	2184	280	201	69	-	-	2142	724	-	-
Ce	2606	8154	3186	6849	994	913	294	-	-	3803	1202	-	-
Pr	378	952	394	1016	126	177	50	-	-	316	91	-	-
Nd	2048	3961	1795	4690	622	1123	299	-	-	997	278	-	-
Sm	638	824	411	1320	164	503	118	-	-	123	33	-	-
Eu	5	26	13	7	4	75	17	-	-	18	4	-	-
Gd	765	752	405	1449	154	689	152	-	-	93	28	-	-
Tb	122	103	56	243	44	104	23	-	-	10	3	-	-
Dy	713	611	295	1554	245	541	121	-	-	72	15	-	-
Ho	135	123	62	309	56	91	20	-	-	16	5	-	-
Er	324	323	159	807	133	171	38	-	-	40	11	-	-
Tm	41	47	20	122	24	15	3	-	-	7	2	-	-
Yb	241	330	152	817	209	117	27	-	-	49	20	-	-
Lu	30	48	22	105	29	25	6	-	-	8	3	-	-
Y	3900	3706	1695	9627	1754	1882	404	-	-	465	86	-	-
Mn	1136	903	101	2362	191	1575	405	-	-	904	115	-	-
Sn	4	0	2	-1	2	0	0	-	-	1	4	-	-
S	366	957	1034	472	777	355	13	-	-	994	833	-	-
No of grains	-	13	-	12	-	13	-	-	-	9	-	-	-

Table 2. Cont.

Sample	WX85NB-11		LG		WX85NB-226		WX85NB-225		WX85NB-188	WX85NB-46	WX85NB-189	DS06-077		WX85NB-38		
Intrusion	Hawkshaw		Lake George		Dungarvon		Dungarvon		Beech Hill	Papineau Falls	Utopia	Long Lake		Allandale		
Mineralization	Cu-Mo		Sn-W		Sn-W		Sn-W		Sn-W	Mo	Mo-Sn	U-Mo		Be-Mo		
No of Grains	3		20		2		6		1	1	6	2		3		
Major elements (wt. %)																
P ₂ O ₅	Av.	1σ	Av.	1σ	Av.	1σ	Av.	1σ	-	-	Av.	1σ	Av.	1σ	Av.	1σ
CaO	42.06	0.2	40.54	2.9	40.61	0.4	40.70	0.5	40.70	39.27	40.41	0.6	42.35	0.7	41.60	0.7
SiO ₂	54.83	0.3	54.23	3.8	53.48	0.0	53.23	0.4	51.85	50.83	53.43	0.2	53.91	0.1	52.77	0.4
FeO	0.38	0.1	0.61	1.2	0.67	0.3	0.40	0.2	0.43	0.75	0.53	0.1	0.31	0.2	0.17	0.1
MnO	0.25	0.1	0.63	1.2	0.58	0.4	0.73	0.1	0.68	2.14	0.80	0.2	0.83	0.5	1.00	0.1
SrO	0.26	0.0	0.11	0.1	0.21	0.0	0.70	0.1	0.57	1.01	0.37	0.0	0.14	0.0	1.58	0.0
Y ₂ O ₃	0.00	0.0	0.01	0.0	0.00	0.0	0.00	0.0	0.00	0.00	0.00	0.0	0.00	0.0	0.00	0.0
Ce ₂ O ₃	0.39	0.1	0.15	0.1	0.89	0.4	0.68	0.2	0.79	0.52	0.88	0.1	0.29	0.0	0.27	0.0
UO ₂	0.13	0.0	0.14	0.1	0.38	0.1	0.28	0.1	0.69	0.19	0.40	0.0	0.09	0.1	0.11	0.0
BaO	0.01	0.0	0.01	0.0	0.00	0.0	0.01	0.0	0.00	0.00	0.00	0.0	0.00	0.0	0.00	0.0
Cl	0.00	0.0	0.01	0.0	0.00	0.0	0.01	0.0	0.00	0.00	0.00	0.0	0.01	0.0	0.00	0.0
F	0.01	0.0	0.05	0.0	0.01	0.0	0.02	0.0	0.02	0.07	0.03	0.0	0.01	0.0	0.04	0.0
SO ₃	3.08	0.4	2.62	0.7	2.81	0.0	3.44	0.3	3.81	3.25	3.24	0.4	2.97	0.2	3.32	0.0
O=F,Cl	0.05	0.0	0.10	0.1	0.00	0.0	0.08	0.2	0.02	0.03	0.01	0.0	0.01	0.0	0.01	0.0
Total	1.30	0.2	1.12	0.3	1.19	0.0	1.45	0.1	1.61	1.38	1.37	0.2	1.25	0.1	1.41	0.0
Trace elements (ppm)																
Sr	100	1	-	-	128	17	52	14	65	-	33	6	-	-	-	-
Th	21	9	-	-	80	19	18	7	88	-	28	12	-	-	-	-
U	35	11	-	-	38	1	14	5	28	-	13	5	-	-	-	-
La	186	62	-	-	812	274	560	47	1191	-	985	156	-	-	-	-
Ce	768	266	-	-	2931	1085	2069	187	5009	-	3576	521	-	-	-	-
Pr	139	44	-	-	507	202	349	28	916	-	531	91	-	-	-	-
Nd	811	249	-	-	2769	1080	1817	190	4994	-	2383	316	-	-	-	-
Sm	389	113	-	-	964	386	878	89	2042	-	852	149	-	-	-	-
Eu	29	6	-	-	10	4	5	4	21	-	5	2	-	-	-	-
Gd	502	150	-	-	1073	433	987	111	2349	-	1091	224	-	-	-	-
Tb	92	29	-	-	188	76	184	17	443	-	201	31	-	-	-	-
Dy	539	178	-	-	1165	470	1026	138	2712	-	1299	214	-	-	-	-
Ho	98	35	-	-	234	92	182	22	503	-	252	42	-	-	-	-
Er	242	90	-	-	655	243	461	57	1302	-	660	102	-	-	-	-
Tm	32	12	-	-	98	34	69	9	178	-	101	23	-	-	-	-
Yb	199	78	-	-	678	218	459	76	1134	-	636	150	-	-	-	-
Lu	25	10	-	-	92	26	60	8	142	-	93	20	-	-	-	-
Y	2639	929	-	-	7950	2828	5162	398	13270	-	7649	1278	-	-	-	-
Mn	2189	295	-	-	1511	288	5893	344	5444	-	3867	226	-	-	-	-
Sn	0	0	-	-	2	2	4	6	0	-	2	2	-	-	-	-
S	358	7	-	-	404	12	582	926	356	-	785	334	-	-	-	-
No of grains	9		-	-	2		14		1	-	6		-	-	-	-

5. Petrographic Study of Apatite Occurrences

Apatite is the most common accessory phase among the Acadian-related granitoids of New Brunswick. In studied samples, apatites are commonly subhedral to euhedral, small (<30 μm) equant crystals enclosed in biotite (Figure 2a), except a few intergranular apatites in samples from the Blue Mountain and Bocabec granites where large (>200 μm to ~1mm) partly resorbed crystals of apatite form phenocrysts (Figure 2b). This may indicate apatite crystal's earlier saturation from the host in most of the samples. The study of Wyllie et al. [74] showed that near-equilibrium growth can commonly produce small equant to subsequent apatite crystals in the presence of a liquid or vapor phase. Apatite necklace in biotite was observed in addition to some regularly sized apatite in the samples from the Lake George Granodiorite (Figure 2c). Most of the examined apatites, with exception of some older intrusions including Utopia and Mount LaTour granites, are not fractured. In the Utopia Granite the examined apatites are enclosed within biotite, which is locally highly altered to chlorite and non-metamict allanite, is a common secondary phase where the alteration is intense (McLeod [66]). Formation of the allanite and monazite inclusions could be attributed to fluid-mediated coupled dissolution-precipitation process (DRP) during the later stages of subsolidus cooling of the granitic intrusion (Putnis [75], Harlov [76,77]). Coupled dissolution-precipitation is a chemical reaction driven by a minimization in the Gibbs free energy (Putnis [75], Harlov [76]). During this process and in the presence of a fluid phase, a mineral phase is replaced either by a new composition of the same phase or by a completely new phase (Putnis [75]). Broom-Fendley et al. [32] used cathodoluminescence (CL) imaging to study DRP processes in apatites, showing different textures and colors of CL emission in zones of any apatite affected by the DRP processes. Most of the examined apatites of this study displayed a homogeneous texture in both SEM-BSE and SEM-CL imaging and show no distinctive changes in the CL-color from core to rim (Figure 3). All the examined apatite grains from Utopia Granite (Mo-bearing) are fractured, show greenish-yellow emission colors and are accompanied by maroon-colored potassium feldspars. These indicate that this intrusion may in fact had been affected by secondary hydrothermal fluid.

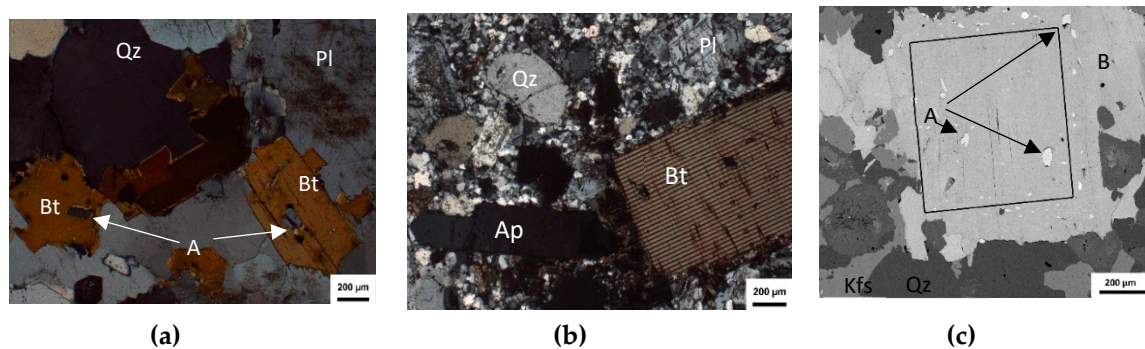


Figure 2. Photomicrographs and SEM-BSE images of some New Brunswick granitoids illustrating the mineralogy and texture of apatite occurrence: (a) Mineral inclusions of apatites in a biotite grain from the Pabineau Falls Granite (WX85NB-46); (b) Partly resorbed apatite phenocryst located in the groundmass close to several resorbed quartz grains and a laser ablated biotite grain in a sample from the Blue Mountain Granite (96-DL-08); (c) Concentric zone of apatite inclusions close to the rim of the host biotite in a sample from the Lake George Granodiorite (LG-1881). Mineral abbreviations after Whitney and Evans [46] where Qz = Quartz, Pl = Plagioclase, Ap = Apatite, Bt = Biotite, and Kfs = K-feldspar.

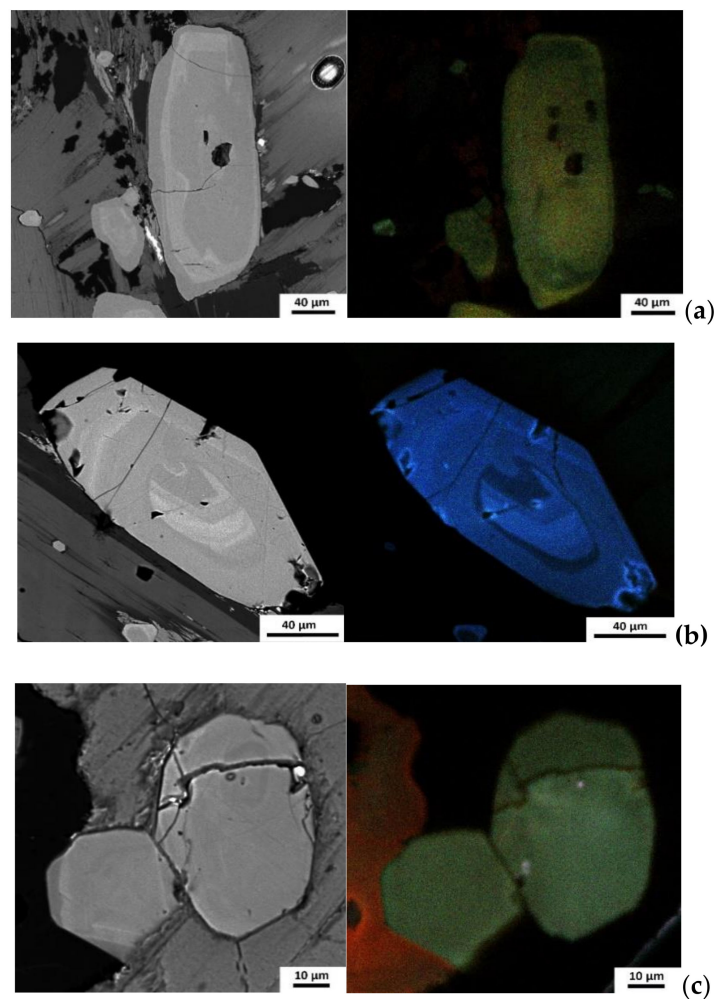


Figure 3. SEM-BSE and SEM-CL images of examined apatite grains: (a) the Lost Lake Granite; (b) the Magaguadavic Granite; (c) Utopia Granite. Note the maroon-colored potassium feldspar, which indicates hydrothermal alteration of the sample.

6. Results

6.1. Apatite Major Elements

6.1.1. Calcium and Phosphorus

Notable variations in P_2O_5 and CaO contents of apatite are evident within the analyzed samples. The P_2O_5 ranges from 38 to 43 wt. %, while CaO varies between 46 and 56 wt. %. Two data points from an altered sample of the Lake George Granodiorite have much lower values in rims compared to their cores for both CaO and P_2O_5 , which may be due to hydrothermal alteration and addition of other components in the samples.

6.1.2. Fluorine and Chlorine

All the studied apatites are categorized as fluorapatite that is common in igneous rocks (Nash [25], Piccoli and Candela [1], Belousova et al. [36]). Fluorine in apatite ranges from 1.2 to 3.0 wt. % (Table 2). In general, Fluorine content of the apatites has a positive correlation with the whole rock SiO_2 content, and it reaches to its highest value of 3.70 wt. % in highly fractionated Dunganvon Granite (Figure 4a). Fluorine content also increases from core to rim in the larger size apatites, which might indicate its response to fractionation of the parent magma. The small apatites in the Lake George Granodiorite samples, where they form the zones along biotite rims, show the lowest F content (less than 2 wt. %)

and the highest OH content (up to 1 wt. %). The barren and Cu-Mo systems contain lower F content (mean value of 2.9 ± 0.6 wt. %) than Sn-W and Mo systems (mean values of 3.3 ± 0.4 and 3.2 ± 0.3 wt. %, respectively; Table 3).

Table 3. Summary of geochemical characteristics in apatites from Acadian-related granitoids of New Brunswick.

	Barren	1s	Cu-Mo System	1s	Sn-W System	1s	Mo Systems	1s
Major elements in wt. % (EPMA)								
CaO	53.7	3.1	53.3	3.6	53.1	0.6	53.1	0.9
P ₂ O ₅	40.5	2.2	40.4	2.5	40.7	0.5	40.8	1.1
SiO ₂	0.7	0.9	0.9	1.6	0.5	0.2	0.4	0.2
MnO	0.3	0.5	0.2	0.1	0.6	0.2	0.7	0.6
FeO	0.7	1.2	0.6	0.8	0.7	0.2	1.0	0.4
F	2.9	0.6	2.9	0.6	3.3	0.4	3.2	0.3
Cl	0.03	0.0	0.12	0.1	0.01	0.0	0.03	0.0
OH	0.4	0.3	0.4	0.3	0.2	0.2	0.3	0.1
Trace elements in ppm (LA-ICP-MS)								
Mn	1582	648.7	1546	696.1	5351	1484.1	3867	226.1
Sr	65	33.2	110	25.4	62	28.4	33	6.2
Y	4925	3540.5	1552	1288.4	5967	2240.7	7649	1278.3
U	117	121.4	31	12.0	18	9.7	13	5.3
Th	133	142.4	64	56.0	29	26.7	28	12.3
Sn	1	1.8	0.25	0.3	4	3.5	3.5	1.5
LREE ¹	11,885	7752.5	4860	3075.8	6450	3606.0	8333	1177.2
HREE ²	8012	3298.0	2563	2128.2	9798	2302.2	11982	1968.5
(La/Yb) _N ³	3.88	3.6	17.61	20.2	0.88	0.1	1.14	0.2
(La/Sm) _N	1.47	1.4	5.85	6.3	0.43	0.1	0.75	0.1
(Eu/Eu*) _N ⁴	0.17	0.2	0.36	0.6	0.02	0.0	0.02	0.0
(Ce/Ce*) _N	1.75	0.6	1.25	0.2	2.24	0.9	2.83	0.3
LREE/HREE	1.64	1.0	5.07	4.8	0.66	0.0	0.70	0.0
fO ₂ ⁵	−13.22	1.3	−13.15	1.5	−21.52	3.3	−18.25	0.5

¹ (La-Eu); ² (Gd-Lu + Y); ³ N = Chondrite normalized. Chondrite REE values from [78]; ⁴ Eu* = (1/2) × Sm_N + (1/2) × Gd_N; ⁵ fO₂ = −0.0022 (± 0.0003) Mn (ppm) − 9.75 (± 0.46).

On the other hand, Cl content of apatites has a negative correlation with the SiO₂ content of the whole rock [79]. Fluorine and Cl are negatively correlated, suggesting that they substitute for one another in the hydroxyl site and that OH is passive (Figure 4b). Chlorine also decreases from core to rim in large apatites, consistent with fractional crystallization of their host magma. Apatites from Cu-Mo systems show much greater Cl content compared to the rest of the samples. These apatites have the greatest mean Cl content (0.12 ± 0.1 wt. %) followed by the apatites from barren, Mo, and Sn-W systems with averages of 0.03 ± 0.01 , 0.02 ± 0.01 , and 0.01 ± 0.01 wt. %, respectively.

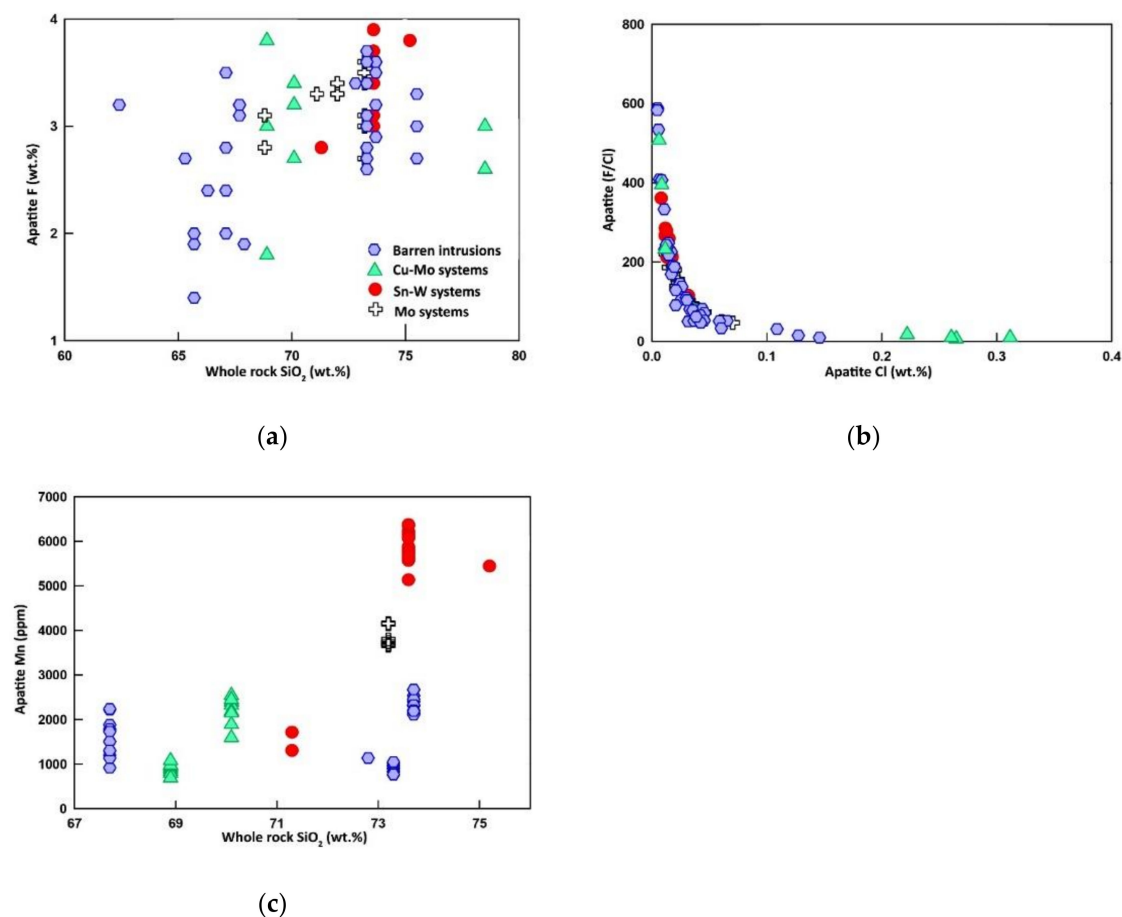


Figure 4. Minor element composition of apatite from barren and mineralized granitoids of New Brunswick: (a) apatite F versus whole rock SiO₂; (b) apatite Cl versus F/Cl; (c) apatite Mn versus whole rock SiO₂.

6.1.3. Silicon

Silicon content of apatite vary markedly among the intrusions; however, most of the samples have values typical of felsic plutonic rocks (<0.8 wt. %; Teiber et al. [26]). The lack of a direct relationship between the whole rock and the apatite silica content indicates a different substitutional mechanism. In general, average silicon content decreases in apatites from Cu-Mo to barren, Sn-W, and Mo bearing systems with 0.9, 0.7, 0.5, and 0.4 wt. %. Our results also indicate increased SiO₂ from core to rim (more than 1 wt. %) for most of the large apatites.

6.1.4. Sulfur

EPMA data show small SO₃ values in apatites, all less than 0.5 wt. %. This result was also confirmed by the LA-ICPMS data; S contents of the analyzed apatites do not exceed 400 ppm and show no distinction between barren and mineralized samples. These SO₃ values (300–400 ppm) are comparable with apatites from more mafic I-type granites (Sha and Chappell [28]), suggesting sulfur occurs as SO₄²⁻ substituting for PO₄³⁻ within the apatite crystal structure in these relatively oxidized I-type granites (Sha and Chappell [28]).

6.1.5. Iron and Manganese

Although FeO contents of apatites are low (<1 wt. %), their average contents increase from 828 ppm in barren granitoids, 1108 ppm in Cu-Mo systems, 2503 ppm to 1108 ppm in Sn-W, and 3574 ppm in Mo systems (see Table 3). Manganese values are almost identical in barren and Cu-Mo systems with

the average of about 1560 ppm. However, the value increases to 3867 ppm in Mo systems and reaches a high of 5351 ppm in Sn-W systems. In general, there is a positive correlation between the whole rock SiO_2 and the apatite Mn contents (Figure 4c). Additionally, Mn content typically increases, but locally decreases from core to rim in some of the examined samples, which might indicate crystallization of other Mn-bearing minerals like magnetite and/or ilmenite in these rocks.

In general, more fractionated, peraluminous I-type granites of New Brunswick (i.e., Sn-W- and Mo-bearing systems) have greater Mn and Fe contents among the studied samples (Table 3). The low oxygen fugacity and peraluminous nature of these intrusions are favorable for more abundant divalent Mn^{2+} and Fe^{2+} cations for substitution in the Ca^{2+} site rather than more highly charged counterparts (Fe^{3+} , Mn^{4+} , and Mn^{6+} ; Sha and Chappell [28]).

6.2. Apatite Trace Elements

6.2.1. Strontium and Yttrium

Strontium values show a wide distribution in the analyzed samples, although it does not exceed 170 ppm. Apatite from the Mo system shows the lowest average value of 33 ppm, which increases to around 65 ppm in both the barren and Sn-W systems, whereas Sr reaches its highest average of 110 ppm in Cu-Mo systems (Table 3). There is also a negative correlation between apatite Sr contents and the whole rock SiO_2 contents (Figure 5a). Yttrium contents show a wide variation among the different rock units and a positive correlation with the SiO_2 content of the whole rock (Figure 5b) and negative correlation with apatite Sr content (Figure 5c). The Y content of apatite increases on average from Cu-Mo to barren, Sn-W, and Mo systems with values of 1500 ± 1290 , 4930 ± 3550 , 5970 ± 2250 , and 7650 ± 1280 ppm, respectively (Table 3). These correlations indicate a Sr decrease, but Y increase through magmatic fractionation in the examined samples (e.g., Cao et al. [15]).

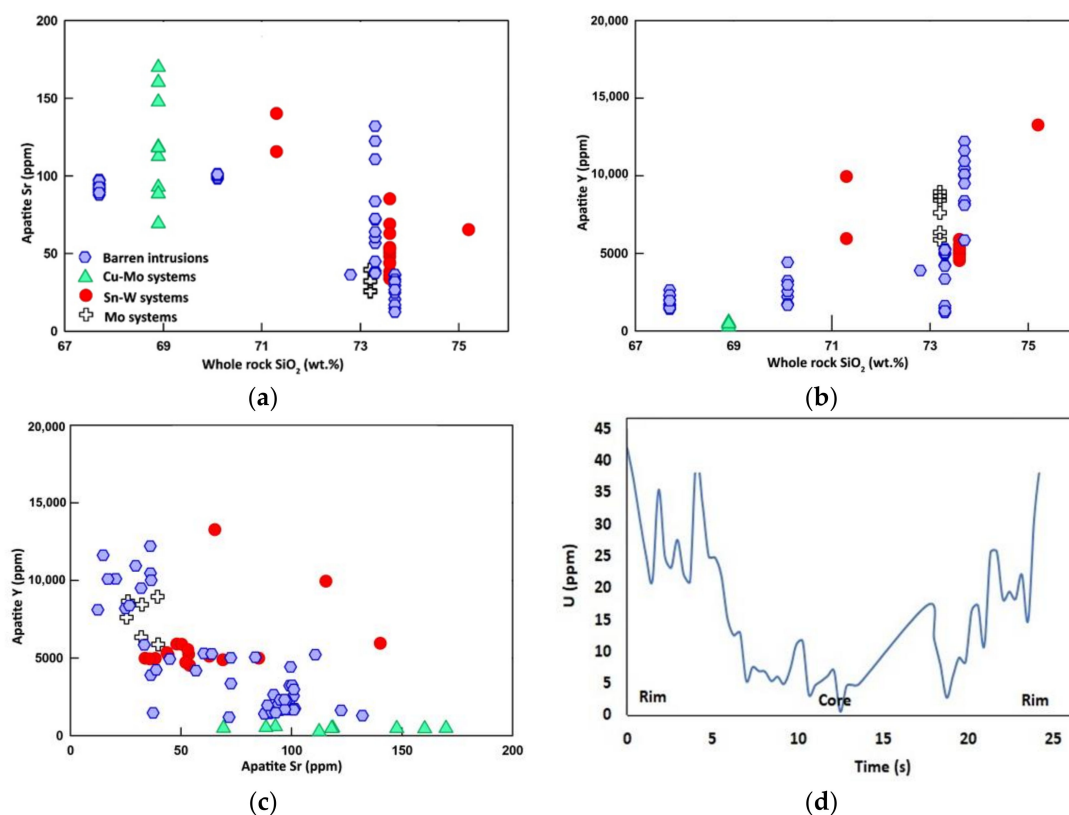


Figure 5. Minor element composition of apatite from barren and mineralized granitoids of New Brunswick: (a) apatite Sr versus whole rock SiO_2 ; (b) apatite Y versus whole rock SiO_2 ; (c) Apatite Y versus Sr; (d) U content variation from rim to rim (1mm) in an apatite from the Mount Douglas Granite.

6.2.2. Uranium and Thorium

Less fractionated, barren intrusions of New Brunswick have the highest U contents averaging 133 ± 122 ppm. Conversely, apatites from the mineralized samples have much lower U contents of around 28–64 ppm on average. Furthermore, U contents of apatite show no direct relationship to the whole rock SiO₂ contents and increases from core to rim in most of the larger grains (Figure 5d). Similarly, apatites from the barren intrusions have the greatest Th values with an average of 117 ± 143 ppm. The average values decrease markedly from 31 ± 56 ppm in Cu-Mo and 18 ± 27 ppm in Sn-W systems to the lowest of 13 ± 12 ppm in apatites from the Mo-related intrusions. There is no direct relationship between the Th contents of apatite and the whole rock SiO₂ contents.

6.2.3. Tin

Tin values vary considerably among the analyzed samples. However, there is an increase in the average Sn values of apatite from Cu-Mo (0.22 ± 0.35) to barren (1.04 ± 1.82 ppm) to Mo (3.48 ± 1.47), and Sn-W (3.92 ± 3.54) related intrusions (Table 3). There is a weak positive correlation between the whole rock SiO₂ and apatite Sn contents.

6.2.4. Rare Earth Elements (REEs)

Analyzed apatite grains have distinctly different REE contents in barren and fertile granitoid samples. The total REE value (Σ REE) increases on average from Cu-Mo, Sn-W, barren and Mo-related intrusions with 5870 ± 2600 , $10,280 \pm 5700$, $11,880 \pm 9000$, and $12,670 \pm 1920$ ppm, respectively (Table 3). This is consistent with the degree of fractionation observed among these granitoid rocks as indexed by increased F, Mn, and Rb/K ratio. Consequently, apatites from the Cu-Mo related intrusions have the weakest Eu anomaly (Eu/Eu* of 0.35 ± 0.20 on average), barren systems have a moderate Eu anomaly of 0.17 ± 0.20 , and finally, Sn-W- and Mo-related systems display the most prominent negative Eu anomaly of 0.01 ± 0.01 . Furthermore, apatites from the granitoids related to different mineral deposits show a variety of chondrite-normalized REE patterns (Figure 5). In general, apatite from mineralized intrusions displays higher chondrite-normalized ratios compared to the apatite from the barren intrusions. Apatite from the least-fractionated member of the barren intrusions (Lost Lake Granite) is characterized by a convex REE pattern ($(La/Yb)_N$ of 1.21) and a weak negative Eu anomaly of 0.38. The more fractionated samples of the group from the Mount Douglas Granite (WX85NB-198 and 220) also show two different patterns. WX85NB-198 shows a slight LREE-enriched pattern with a stronger negative Eu anomaly of 0.10, while sample WX85NB-220 shows an almost flat gullwing shape with a more pronounced negative Eu anomaly of 0.01 (Figure 6a–c). Apatite from the Cu-Mo systems also display two different chondrite-normalized REE patterns. Apatites from the Magaguadavic Granite displays LREE-enriched patterns with a small negative Eu anomaly of 0.51. In contrast, apatites from the Hawkshaw Granite shows a convex pattern with a more pronounced negative Eu anomaly (Eu/Eu* of 0.20; Figure 6d,e). Apatite from the Sn-W-related intrusions shows an almost flattened gullwing shaped REE pattern ($(La/Yb)_N$ of 0.81) and strong negative Eu anomalies of about 0.02 on average (Figure 6f–h). Lastly, apatite grains from the Utopia Granite, the only Mo-related intrusion we studied, displays a similar pattern to the Sn-W-related intrusions with a deep negative Eu anomaly of 0.01, and small positive Ce anomalies.

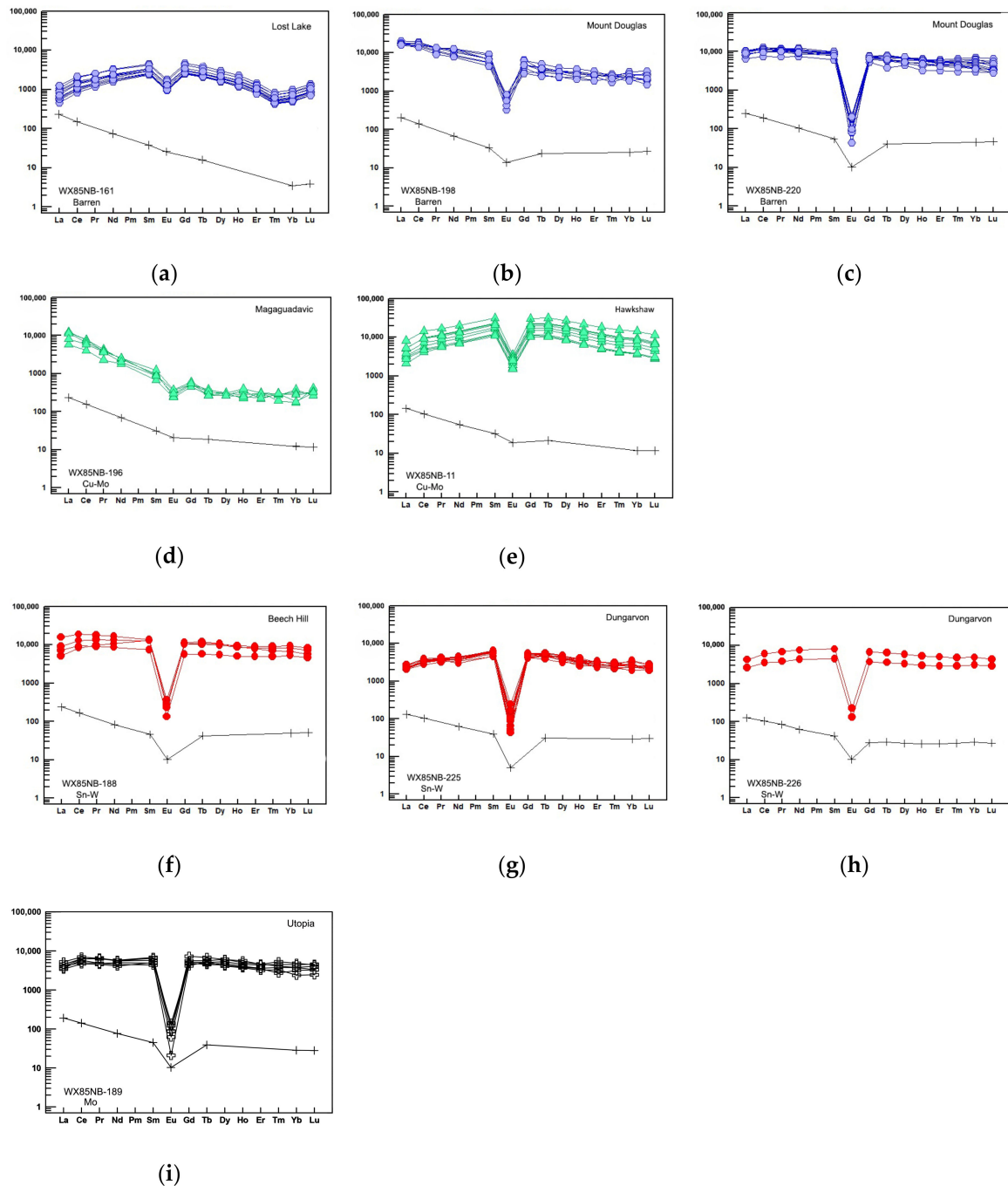
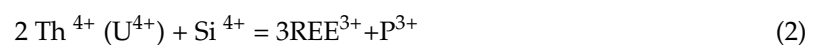


Figure 6. Chondrite-normalized apatite REE patterns of apatites (colored lines with filled symbols) and their host rocks (black with + symbols) for Acadian granitoids of New Brunswick (black lines with + symbols). (a) Lost Lake Granite, (b, c) Mount Douglas Granite (Dmd₁), (d) Magaguadavic Granite, (e) Hawkshaw Granite, (f) Beech Hill Granite, (g, h) Dungarvon Granite, (i) Utopia Granite: Chondrite REE values from Sun and McDonough [78].

7. Discussion

The REE abundance of each mineral depends on its compatibility relationships, the sequence of crystallization, and partitioning of the elements between the minerals and melt. Titanite and magnetite are common Ti-bearing minerals in oxidized I-type granites. High Ca, oxidized melt also favors allanite saturation. Thus, apatite, titanite, and allanite crystallization controls the behavior of LREE in all but the most felsic I-type granites.

All the examined intrusions have similar Th and U whole rock contents, so that the contrast observed in U and Th contents of apatite grains in barren and mineralized granitoid samples are not due to whole rock (melt) differences, but to competing Th + U-bearing accessory phases. Monazite, for instance, preferentially incorporates Th over U with Th/U of 20–25 in S-type and ~4 in I-type granites (Sha and Chappell [28]); however, monazite is a common accessory phase in peraluminous fractionated I-type granites (Mo- and Sn-W-bearing granites) and is not observed among the less fractionated I-type granites (Barren and Cu-Mo-related intrusions) of New Brunswick. Other phases must be competing for U and Th in the New Brunswick systems. Both U and Th occur almost exclusively as tetravalent elements (e.g., U^{4+} and Th^{4+}) in the igneous environment (Robb [80]) and enter apatite crystal structure by a variety of complex substitutions (Pan and Fleet [2], Li et al. [81]). Thorium and U may substitute within apatite crystal structure by any of the following (Casillas et al. [82]):



As shown in Figure 7, Th and U show a good correlation with Si and REE + Y, indicating that substitutions 2 and 3 play a more important role in substituting U and Th within the apatite crystal structure rather than substitution 1. Bea et al. [83] measured high partition coefficient values (phenocryst-groundmass) for both U ($K_D = 43.7$) and Th ($K_D = 41$) for apatites from strongly differentiated peraluminous perphosphorus granites of the Pedrobernardo pluton in central Spain. The partition coefficient values of the examined apatite were calculated for both U and Th using apatite trace element composition and taking whole rock data as the representative of the melt composition. The calculated results in this study were much lower and variable with U partition coefficient varying from 0.50 to 22.25 and Th partition coefficient varying from 0.20 to 15.85. Partition coefficient values should be approached with caution as Nernst partition coefficient can be affected by composition and oxygen activity of the melt, temperature, and pressure (Fujimaki [84], Rollinson [85]) and the important and tenuous assumption that the rock represents a melt composition from which the apatite crystallized. It is hard to fractionate apatite (specific gravity) from the melt-magma (specific gravity of 2.3 g/cm^3). Apatite can fractionate from early to late if it is saturated in the melt, although the crystals are so fine, they tend to not physically separate from the melts, but rather are entrained in that higher viscosity melt, except under rare circumstances. Our samples are less fractionated, compared with those of Bea et al. [83], are I-type, and are not perphosphoric; these facts may explain the different partition coefficient values observed.

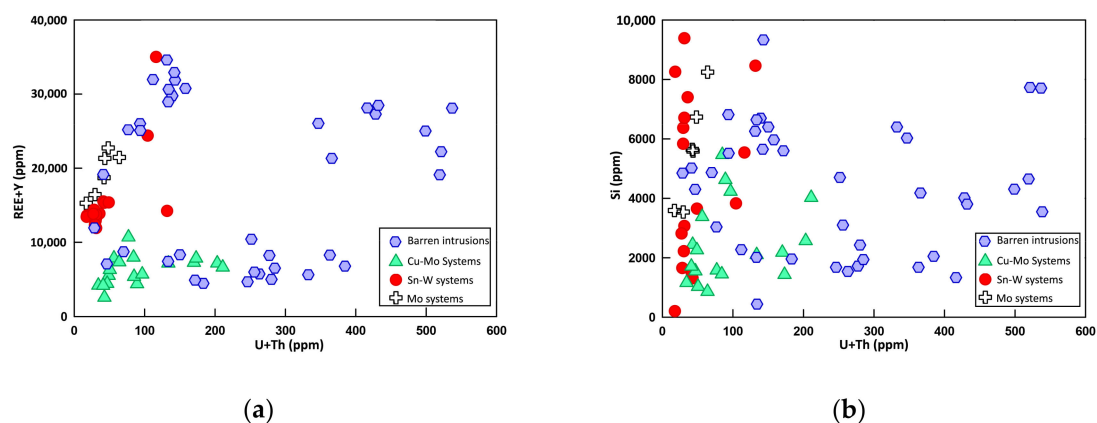


Figure 7. Apatite compositions from the Acadian-related granitoids of New Brunswick. (a) Plot of Th + U versus REE + Y variation; (b) plot of Th + U versus Si.

Apatite from the barren intrusion contains the most abundant LREE ($\Sigma\text{La-Sm}$) with the average of about 12,000 ppm compared to the grains from mineralized intrusions with less than 10,000 ppm LREE. Mafic (SiO_2 between 57–70 wt. %) and felsic I-type granites ($\text{SiO}_2 > 70$ wt. %) have almost the same REE contents and whole-rock REE patterns, except for highly fractionated I-type granites (Sha and Chappell [28]). Therefore, the differences in apatite TE composition is not melt (rock) composition controlled but depend on internal redistribution of the melt load to REE-bearing minerals during fractional crystallization (Sha and Chappell [28]). Apatite, zircon, titanite, ilmenite, and perhaps allanite are the major REE-bearing minerals in less evolved I-type granitic rocks (tonalites and granodiorites), whereas plagioclase, K-feldspar, monazite, xenotime, zircon, and apatite are common REE-bearing minerals in felsic I-type granites *sensu stricto*. Mafic I-type granites are more oxidized and metaluminous compared to felsic I-type granites. Monazite solubility decreases with increasing aluminum saturation index (ASI) in the metaluminous environment (Montel [86]). Consequently, monazite becomes less readily saturated in less evolved I-type granitoid rocks. Furthermore, high Ca content of these granitoids (magmas) would enhance an early saturation of apatite, which results in REE depletion and would further postpone the saturation of monazite (Sha and Chappell [28]).

7.1. Source of Hydrothermal Fluids (F, Cl)

All the examined apatites from this study of granites are classified as fluorapatites. Fluorine is more compatible in silicate melts comparing to fluids during fractional crystallization (Piccoli and Candela [1], Ding et al. [30]) and given that apatite is an early crystallizing phase in many systems, they take up the melt-available-F. Apatites in Cu-Mo systems have high Cl and low F contents compared to the other apatites (Figure 4b) so how do they achieve this higher Cl/F ratio. Webster et al. [87] showed by experiment that Cl has a partition coefficient of 1.0 to 4.5 between apatite and granitic melts (i.e., neutral to modest strong compatibility). Chlorine is highly compatible with apatite in Cl-saturated melts, but if the system is water saturated, Cl would preferentially partition into the aqueous fluid instead of the silicate melt and this mechanism is probably a strong controller in fluid saturated (moderately felsic) melts and not fractional crystallization (i.e., evolved magmas could have the same or even increase Cl content of the parent magma; Ding et al. [30]). Previous studies have shown that magma concentration of Cl in basalts varies in different source regions, but that tectonic Cl recycling is not a significant driver (Ding et al. [30]). Furthermore, experimental work on glass inclusions interpreted as melt compositions from both melt inclusions (Lassiter et al. [88]) and submarine volcanic glasses (Stroncik and Haase [89]) suggest that the mantle commonly contains low abundances of Cl (<0.1 wt. %). The relatively high concentration of Cl in the Cu-Mo related granites of New Brunswick cannot be produced from the addition of mantle compositions (e.g., Ding et al. [30]). These high Cl/F are also difficult to achieve by partial melting of crustal material, especially given sediments lose their Cl content during weathering (witness sea water compositions; Blevin and Chappell [90]). As a result, Cl must have been provided by a fluid component (ligand) in Cu-Mo related intrusions of New Brunswick. Dehydration of sediments on the subducting slab can advance melting of mantle wedge by releasing mainly Cl-rich brines (Lassiter et al. [88], Ding et al. [30]). The experiments of Candela and Holland [91] and Eugster [92] clearly showed the effect of Cl on Sn^{2+} transportation and a combination of F, OH, and Cl on Mo^{4+} , Mo^{6+} , and W^{4+} transportation in granitic systems. Depending a slab dehydration, however, this does not explain halogen behaviour Sn-W- and Mo-bearing granites in an intraplate setting (Ding et al. [30]).

7.2. Oxidation State

Cerium, Eu, and Mn are three elements with variable oxidation states that substitute in apatite in significant quantities. As a result, many researchers have used these elements to estimate the oxidation state of the host magma (Sha and Chappell [28], Belousova et al. [36], Cao et al. [15], Miles et al. [16], Ding et al. [30], Marks et al. [3]). Although Eu incorporation in apatite is mainly controlled by the oxidation state of the magma, it is also strongly affected by feldspar fractionation on the melt

composition (Belousova et al. [36]). Apatite crystal structure itself is a controlling factor. Europium has two valences of Eu^{2+} and Eu^{3+} , which allow it to substitute for Ca^{2+} in both the seven and nine-fold coordinated positions within apatite crystal structure (Sha and Chappell [28], Cao et al. [15]). Eu^{3+} has a smaller effective ionic radius (1.01 and 1.12 Å) compared to both seven and nine-fold Ca^{2+} (1.06 and 1.18 Å, respectively) in apatite. Therefore, Eu^{3+} preferentially substitutes for Ca^{2+} in apatite rather than Eu^{2+} , which preferentially substitutes for Ca in plagioclase (Sha and Chappell [28], Cao et al. [15]). In addition to the whole-rock (magma) oxidation state, $\text{Eu}^{2+}/\text{Eu}^{3+}$, and $\text{Ce}^{3+}/\text{Ce}^{4+}$ in both melt and mineral composition (i.e., apatite) are strongly affected by whole-rock composition, temperature, and possibly pressure (Cao et al. [15]). Therefore, low oxygen fugacity of the magma results in high $\text{Eu}^{2+}/\text{Eu}^{3+}$ and $\text{Ce}^{3+}/\text{Ce}^{4+}$, increasing availability of Ce^{3+} to be incorporated by apatite. This would lead to a considerable partitioning of Ce^{3+} and limited Eu^{3+} into the apatite structure causing a strong negative Eu and a positive Ce anomaly. Cao et al. [15] emphasized that $(\text{Eu}/\text{Eu}^*)_{\text{N}}$ ratio where Eu^* is the value intermediate to normalized Sm and Gd, (i.e., gives a smooth chondrite-normalized pattern), can better reflect the oxidation state of the host compared with $(\text{Ce}/\text{Ce}^*)_{\text{N}}$. They concluded deep anomalies of $(\text{Eu}/\text{Eu}^*)_{\text{N}}$ ratio represents a more reduced environment, whereas a weak to moderate anomaly represents a more oxidized environment. Apatite from the Sn-W-related intrusions including the Dungarvon and Beech Hill granites show the most pronounced negative anomalies with $(\text{Eu}/\text{Eu}^*)_{\text{N}}$ of 0.004 to 0.02, reflecting the reduced nature of their respective hosts (Figure 8). Apatite grains from the Mo-bearing Utopia Granite also plot close to those from Sn-W related intrusions. However, Mo mineralization is commonly associated with an oxidized environment (Blevin and Chappell [90], Vigneresse [93]). Early crystallization of sufficient plagioclase prior to apatite could lower Eu content and result in an Eu-depleted residual melt. Consequently, apatites of these systems can show much more pronounced negative Eu anomalies (Ding et al. [30]). Conversely, apatite from the Cu-Mo systems and barren intrusions shows a greater ratio of 0.11 to 0.85, reflecting the more oxidized nature of their hosts. Interestingly, apatite grains from the Magaguadavic intrusion have the greatest $(\text{Eu}/\text{Eu}^*)_{\text{N}}$ ratio of 0.41 to 0.85 reflecting the highly oxidized nature of this Cu-Mo related intrusion (Figure 8). These results agree with the color of the host biotite where apatites with the lowest Eu anomalies resides in reddish brown biotites, while grains with the high ratio are enclosed in greenish brown biotites where the biotite's color is thought to reflect its ferrous/ferric ratio (cf. Lalonde and Bernard [94]).

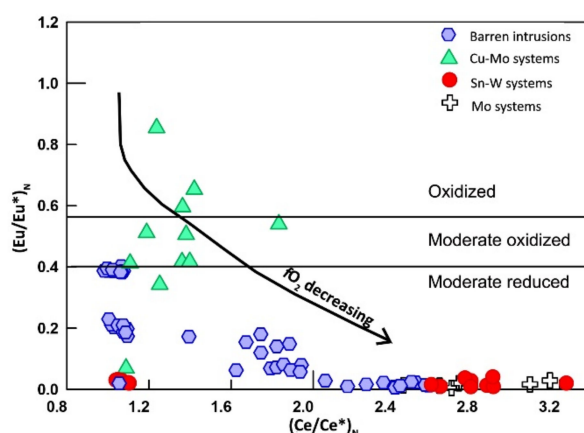


Figure 8. Apatite Eu anomalies versus Ce anomalies where $(\text{Eu}/\text{Eu}^*)_{\text{N}} = \text{Eu}_{\text{N}} / [(1/2) \cdot \text{Sm}_{\text{N}} + (1/2) \cdot \text{Gd}_{\text{N}}]$ and $(\text{Ce}/\text{Ce}^*)_{\text{N}} = \text{Ce}_{\text{N}} / [(1/2) \cdot \text{Sm}_{\text{N}} + (1/2) \cdot \text{Pr}_{\text{N}}]$.

The oxygen fugacity of a magma reflects not only the source, but also its tectonic environment (Cao et al. [15], Ding et al. [30]). Previous studies suggest oxidized magma (I-type granite) come from mantle constituents or slab melting, whereas reduced magmas (S-type granite) are from partial melting of the upper crust (Ishihara [95], Belvin and Chappell [90], Ding et al. [30]). Therefore, the deep Eu anomalies of apatite from the Magaguadavic intrusion may suggest that they have formed from an oxidized magma that incorporated some fraction of mantle-derived material. Interestingly,

this intrusion includes abundant irregular mafic pods and xenoliths, which may confirm the mantle contribution in the source (McLeod [66]). This is confirmed by the positive ϵ_{Nd} value of 1.5 that might indicate a mantle-derived source for this intrusion (Whalen [42], Whalen et al. [58]). Apatites from the barren granites display deeper Eu anomalies, suggesting formation under a moderate oxygen fugacity condition and a mixture of a mantle and crust contributions in the source. Lastly, the low ratio of Eu anomalies in apatite from the highly fractionated Sn-W related intrusion suggests that they formed by a reduced magma derived from partial melting of the crustal material with limited mantle input.

The arguments above are bolstered by other multivalent constituents. Reduced systems should have higher Mn content due to the close similarity of Mn^{2+} in ionic radius and valence to Ca^{2+} than Mn^{3+} and Mn^{4+} (Belousova et al. [36]). Miles et al. [16] presented an equation using Mn in apatite as an oxybarometer in intermediate and silicic igneous rocks. Their study indicated that the oxygen fugacity of the host magma could be calculated following Equation (4):

$$\log fO_2 = -0.0022 (\pm 0.0003) \text{ Mn (ppm)} - 9.75 (\pm 0.46), \quad (4)$$

Using this to calculate fO_2 for the current study indicates similar oxygen fugacity for barren and Cu-Mo related intrusions with an average $\log fO_2$ value of about -13.2 atm (in hematite-magnetite domain (Hm-Mt) [21]). Apatites from the Mo deposits shows a moderately lower oxygen fugacity with the average of -18.2 atm (between quartz-fayalite-magnetite and nickel-nickel oxide). Conversely, apatites from the Sn-W related intrusions lead to a much lower oxygen fugacity of -21.5 atm (within methane-carbon dioxide domain), consistent with a reduced nature of these granitoids. However, the results are not in agreement with the Eu anomalies. For example, oxygen fugacity of the apatites from the Mount Douglas Granite was calculated to be around -11 atm (above hematite-magnetite line [21]), which represent an oxidized environment. This contrast with its highly reduced features like brown biotite and its association with Sn mineralization. Interestingly, Marks et al. [3] indicated that using Mn as an oxybarometer may not be as simple as it looks, because oxygen fugacity is strongly dependent on temperature. They concluded that for at least some rock types, other parameters like the presence/absence of other Mn-bearing phases and melt composition must have an important effect on Equation (4).

7.3. Petrogenesis

The REE pattern, Sr, and Eu anomalies of apatite are interpreted to reflect the compositional evolution of the host magma and can be used as an indicator of compositional heterogeneity or magma mixing and the fractionation of the magma source (Chu et al. [29]). Furthermore, the Sr content of apatite reflects the Sr content of the crystallizing system. For example, Sr partition coefficient of apatite varies from 1.1 to 1.3 in basanite-basalt, 1.3 to 1.4 in tholeiite-andesite, 2.1 to 2.4 in granitic systems, and 0.85 to 2.4 in carbonatites (Watson and Green [96], Dawson and Hinton [97], Klemme and Dalpé [98]). Apatite Sr content is typically less than of the host and rarely exceeds 200 ppm in granitic rocks (Chu et al. [29]). All the examined apatites have lower Sr contents in comparison with their host and does not exceed 170 ppm. The Lost Lake Granite, the least fractionated member of the barren intrusions, displays a convex REE pattern with a small Eu anomaly. Additionally, apatite La/Sm ratio is not considerably influenced by either fractional crystallization or partial melting. However, it is significantly controlled by the amount of melting of subducted oceanic sediments (Turner and Foden [99], Labanieh et al. [100], Ding et al. [30]). As a result, an increase in the amount of sedimentary melting would increase the range of La/Sm ratio of apatite. This would also increase the Th content that in part lowers the apatite Sr/Th ratio (Ding et al. [30]). In contrast, addition of fluid derived from dehydration of subducting slab will stabilize La/Sm ratios but increase the range of Sr/Th ratios in the resulting magmas (Ding et al. [30]). These two processes can be recognized using Sr/Th vs. La/Sm binary plot (Figure 8). Apatites from the barren intrusions also show evidence consistent with oxidized melts derived from subducting slab dehydration (Figure 8) and their high Eu

anomalies also reflect the oxidized nature of the melt and record formation in a magmatic arc related to an oceanic plate subduction environment (Belvin and Chappell [79,90], Belvin [101], Imai [38], Cao et al. [15], Ding et al. [30]). In contrast, apatite in the highly fractionated member of the barren intrusions (the Dmd₁ phase of the Mount Douglas Granite) shows a distinctly different trace-element composition, chondrite-normalized REE patterns, prominent negative Eu anomalies, and higher F/Cl and La/Sm ratios. This is interpreted to reflect the reduced environment of the host, suggesting that the reduced magma was produced by partial melting of crustal material with limited oxidized supra subduction mantle input (Figure 9).

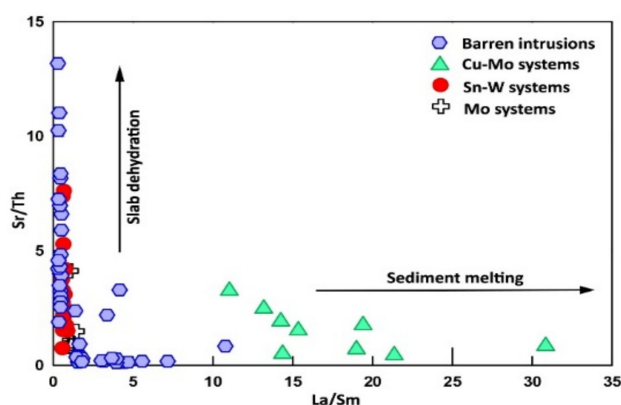


Figure 9. Sr/Th versus La/Sm for apatites from granitoids of New Brunswick.

The apatites from the Cu-Mo related intrusions show less variations in terms of both major- and trace-element compositions compared with the barren counterparts (Tables 2 and 3). The two members of this group have a different degree of fractionation reflected by their chondrite-normalized REE patterns and Eu anomalies. The Magaguadavic Granite, the least fractionated member of the group, displays a LREE-enriched pattern with a moderate negative Eu anomaly. It also shows evidence of sedimentary melting in its source (Figure 8). The moderate Eu anomaly of these apatites records an oxidizing, perhaps subduction zone, environment for the host. However, sedimentary re-melting has contributed to its source reflected by its high La/Sm ratio.

Conversely, Mo-related Utopia Granite, has an almost flat REE pattern with a deep negative Eu anomaly reflecting the fractionated nature of its host magma. However, the deep negative Eu anomalies of apatites from this intrusion may refer to abundant plagioclase fractionation prior to the apatite crystallization. REE elements are among the least mobile elements; although, they might be mobilized through secondary hydrothermal alteration and fluid interaction, if the host REE-bearing mineral becomes altered, whereas the rest of the host rock remained inert (Exley [102]).

Strontium is a more mobile element compared with the REE elements (Exley [102]); therefore, the Sr values of the apatite should be lower than normal if the apatite has been altered. Interestingly, all the examined apatites from the Utopia Granite have much lower Sr content (average of 35 ppm) compared with apatites from other intrusions (average of about 100 ppm). These observations may suggest that apatite from the Utopia Granites have been hydrothermally altered in a way that some of the REE elements redistributed from apatite to allanite (or monazite).

Lastly, several lines of evidence including almost identical major- and trace-element contents including Sr, Mn, and Y in addition to the REE patterns among the apatites from the Sn-W related intrusions suggest a similar magmatic source for these intrusions. The flat REE pattern and strong negative Eu anomalies of these intrusions reflect the highly fractionated nature and reduced environment of the evolved magmas (cf. Cao et al. [15], Ding et al. [30]). Their high F/Cl ratios also suggest re-melting of sedimentary rocks in their source (Cao et al. [15]). As a result, they may have formed mainly from partial melting of crustal material with limited mantle input in an arc environment.

7.4. The Potential Detector of Mineralization

The results of this study indicate that magmatic apatite from barren, Cu-Mo, Sn-W, and Mo related intrusions have distinctly different geochemical characteristics, which can be used to differentiate their associated mineral deposits. For example, apatite from the Sn-W related intrusions have the highest Mn, Fe, Y, Th, Sn, and Σ REE contents and display the deepest negative Eu anomaly. Plots of Sr versus Mn, Sr versus LREE/HREE, and Mn versus $(La/Yb)_N$, and Mn versus $(Eu/Eu^*)_N$ allow classification of apatite compositions for granitoid rocks associated with different mineralization types (Figure 10). The Sr and Mn contents of apatites vary markedly among the samples and display a negative correlation (Figure 10a), reflecting the degree of fractionation of the host magmas. A weaker correlation is observed between Sr contents versus LREE/HREE ratios of apatite, but it still can be used to differentiate different mineral deposits (Figure 10b). Apatites from highly differentiated granites and pegmatites are characterized by extreme LREE depletion relative to the HREE, while apatites from more mafic counterparts are characterized by a stronger LREE enrichment (Belousova et al. [36]). Furthermore, Mn versus $(La/Yb)_N$ displays a negative correlation. The slope of the REE pattern increases from granites and pegmatites toward intermediate, mafic and reaches to its steepest in ultramafic rocks with no direct relationship to the total REE content (Belousova et al. [36]). Mn versus the Eu anomaly displays a strong negative correlation, reflecting degree of magmatic fractionation (Figure 10d).

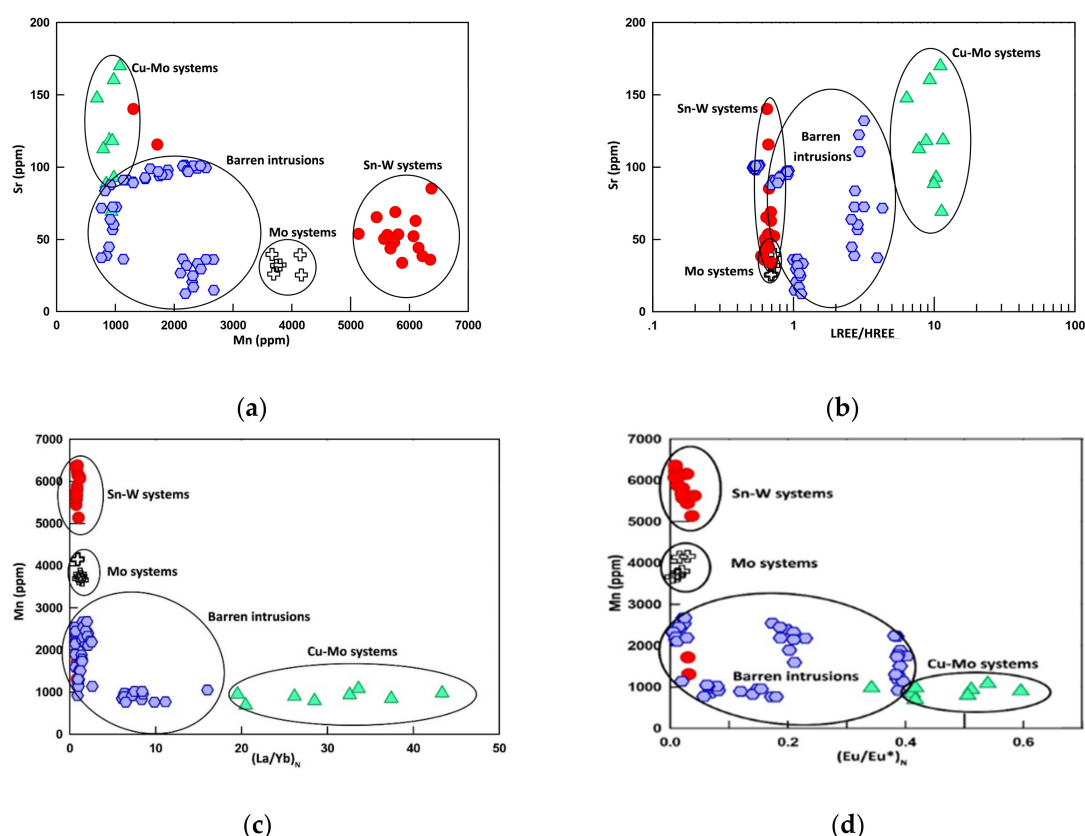


Figure 10. Trace element discrimination plots for apatites from Acadian-related granitoids of New Brunswick: (a) Mn versus Sr; (b) LREE versus Sr; (c) $(La/Yb)_N$ versus Mn; (d) $(Eu/Eu^*)_N$ versus Mn.

8. Conclusions

Apatite composition is an excellent fertility index that can be used as an exploration tool to distinguish barren and mineralized reduced or mineralized-oxidized felsic intrusions as shown in this study. We used a combination of electron probe microanalysis and laser ablation-inductively coupled

plasma-mass spectrometry major- and trace-element apatite data for both barren and mineralized magmatic suites of Acadian-related granitoids of New Brunswick and can be assigned characteristic apatite signatures to types of metallogenic fertility. Apatites from the Cu-Mo related intrusions have the shallowest negative Eu/Eu* (mean of 0.36 ± 0.60) and lowest positive Ce/Ce* (mean of 1.25 ± 0.20) among the analyzed grains, suggesting that they may have incorporated mantle-derived material in oxidized magmas. Apatites from barren intrusions have moderate Eu/Eu* (mean of 0.17 ± 0.20) and Ce/Ce* (mean of 1.67 ± 0.63), suggesting they host formed under moderate-oxygen-fugacity conditions and contained less mantle-derived and more crust-derived material. Lastly, apatites from Sn-W have the deepest negative Eu/Eu* (mean of 0.02 ± 0.01) and the highest positive Ce/Ce* (mean of 2.24 ± 0.90) among the analyzed samples, suggesting that these granites may have formed from a reduced magma derived from partial melting of crustal material with limited mantle input.

The results of the study indicate that apatite Mn, Sr, and LREE/HREE ratios can be used as fertility indices. The apatite grains from the Mo systems have the lowest SiO₂ (<0.4 wt. %), Sr (<33 ppm), Th (<28 ppm), a moderate Mn (~3800 ppm), Y (~3500 ppm), and highest FeO (<0.9 wt. %). Sn-W related magmatic suites have the highest F (>3 wt. %), Mn (>5350 ppm), Fe (>2200 ppm), Y (>4900 ppm), Sn (>2 ppm), and the lowest Cl (<0.01 wt. %), Sr (<60 ppm), U (<18 ppm), Th (<29 ppm), (Eu/Eu*)_N ratios (<0.01), and (La/Yb)_N ratios (<0.88). Conversely, apatite grains from the Cu-Mo related intrusions are classified by their highest Cl (>0.1 wt. %), (La/Yb)_N ratios of 21.17, (Eu/Eu*)_N ratios of 0.3, and LREE/HREE ratios of 6.03. Apatite grains from the barren intrusions are the most hydrous grains (OH > 0.3 wt. %), and lowest Mn (<1700 ppm), Fe (<800 ppm), and Sn (<0.01 ppm).

Author Contributions: Conceptualization, Z.A. and D.R.L.; Methodology, Z.A.; software, Z.A.; Writing-Original Draft Preparation, Z.A.; Review and Editing, D.R.L. and C.R.M.M.

Funding: This project was financed in part by the Geological Survey of Canada as a part of the Targeted Geoscience Initiative (TGI) program, and by a grant from Natural Resources Canada, and a Natural Sciences and Engineering Research Council (NSERC) Discovery grants to David R. Lentz and Christopher McFarlane.

Acknowledgments: The authors thank the many people and organizations who support this research. In particular, we thank Neil Rogers and Joseph Whalen of the Geological Survey of Canada and the staff of the New Brunswick Department of Energy and Resource Development. We thank Douglas Hall and Brandon Boucher of UNB for their help with collecting the geochemical data.

Conflicts of Interest: The authors declare no conflicts of interest.

References

1. Piccoli, P.M.; Candela, P.A. Apatite in igneous systems. *Rev. Miner. Geochem.* **2002**, *48*, 255–292. [[CrossRef](#)]
2. Pan, Y.; Fleet, M.E. Compositions of the apatite-group minerals: Substitution mechanisms and controlling factors. *Rev. Miner. Geochem.* **2002**, *48*, 13–49. [[CrossRef](#)]
3. Marks, M.A.; Scharrer, M.; Ladenburger, S.; Markl, G. Comment on “Apatite: A new redox proxy for silicic magmas?” [*Geochimica et Cosmochimica Acta* 132 (2014) 101–119]. *Geochim. Cosmochim. Acta* **2016**, *183*, 267–270. [[CrossRef](#)]
4. Hughes, J.M.; Maryellen, C.; Mariano, A.D. Rare-earth-element ordering and structural variations in natural rare-earth bearing apatites. *Am. Miner.* **1991**, *76*, 1165–1173.
5. Toplis, M.J.; Dingwell, D.B. The variable influence of P₂O₅ on the viscosity of melts of differing alkali/aluminium ratio: Implications for the structural role of phosphorus in silicate melts. *Geochim. Cosmochim. Acta* **1996**, *60*, 4107–4121. [[CrossRef](#)]
6. Lisowiec, K.; Slaby, E.; Götze, J. Cathodoluminescence (CL) of apatite as an insight into magma mixing in the granitoid pluton of Karkonosze, Poland. In Proceedings of the Conference on Raman and Luminescence Spectroscopy in the Earth Sciences, Wien, Austria, 3–6 July 2013.
7. Nemchin, A.A.; Pidgeon, R.T. U-Pb ages on titanite and apatite from the Darling Range granite: Implications for Late Archaean history of the southwestern Yilgarn Craton. *Precambrian Res.* **1999**, *96*, 125–139. [[CrossRef](#)]
8. Chamberlain, K.R.; Bowring, S.A. Apatite–feldspar U-Pb thermochronometer: A reliable, mid-range (450 °C), diffusion-controlled system. *Chem. Geol.* **2001**, *172*, 173–200. [[CrossRef](#)]

9. Gleadow, A.J.; Kohn, B.P.; Brown, R.W.; O'Sullivan, P.B.; Raza, A. Fission track thermotectonic imaging of the Australian continent. *Tectonophysics* **2002**, *349*, 5–21. [[CrossRef](#)]
10. Harrison, T.M.; Catlos, E.J.; Montel, J.-M. U-Th-Pb dating of phosphate minerals. *Rev. Miner. Geochem.* **2002**, *48*, 524–558. [[CrossRef](#)]
11. Carrapa, B.; DeCelles, P.G.; Reiners, P.W.; Gehrels, G.E.; Sudo, M. Apatite triple dating and white mica $^{40}\text{Ar}/^{39}\text{Ar}$ thermochronology of syntectonic detritus in the Central Andes: A multiphase tectonothermal history. *Geology* **2009**, *37*, 407–410. [[CrossRef](#)]
12. Chew, D.M.; Sylvester, P.J.; Tubrett, M.N. U-Pb and Th-Pb dating of apatite by LA-ICPMS. *Chem. Geol.* **2011**, *280*, 200–216. [[CrossRef](#)]
13. Tang, M.; Wang, X.-L.; Xu, X.-S.; Zhu, C.; Cheng, T.; Yu, Y. Neoproterozoic subducted materials in the generation of Mesozoic Luzong volcanic rocks: Evidence from apatite geochemistry and Hf-Nd isotopic decoupling. *Gondwana Res.* **2012**, *21*, 266–280. [[CrossRef](#)]
14. Vamvaka, A.; Siebel, W.; Chen, F.; Rohrmüller, J. Apatite fission-track dating and low-temperature history of the Bavarian Forest (southern Bohemian Massif). *Int. J. Earth Sci.* **2014**, *103*, 103–119. [[CrossRef](#)]
15. Cao, M.; Li, G.; Qin, K.; Seitmuratova, E.Y.; Liu, Y. Major and trace element characteristics of apatites in granitoids from Central Kazakhstan: Implications for petrogenesis and mineralization. *Resour. Geol.* **2012**, *62*, 63–83. [[CrossRef](#)]
16. Miles, A.J.; Graham, C.M.; Hawkesworth, C.J.; Gillespie, M.R.; Hinton, R.W.; Bromiley, G.D. Apatite: A new redox proxy for silicic magmas? *Geochim. Cosmochim. Acta* **2014**, *132*, 101–119. [[CrossRef](#)]
17. Zhu, C.; Sverjensky, D.A. F-Cl-OH partitioning between biotite and apatite. *Geochim. Cosmochim. Acta* **1992**, *56*, 3435–3467. [[CrossRef](#)]
18. Teiber, H.; Marks, M.A.; Wenzel, T.; Siebel, W.; Altherr, R.; Markl, G. The distribution of halogens (F, Cl, Br) in granitoid rocks. *Chem. Geol.* **2014**, *374*, 92–109. [[CrossRef](#)]
19. Stormer, J.C.; Carmichael, I.S.E. Fluorine-hydroxyl exchange in apatite and biotite: A potential igneous geothermometer. *Contrib. Miner. Petrol.* **1971**, *31*, 121–131. [[CrossRef](#)]
20. Ludington, S. The biotite-apatite geothermometer revisited. *Am. Miner.* **1978**, *63*, 551–553.
21. Wones, D.R. Contributions of crystallography, mineralogy, and petrology to the geology of the Lucerne pluton, Hancock County, Maine. *Am. Miner.* **1980**, *65*, 411–437.
22. Munoz, J.L. F-OH and Cl-OH exchange in micas with applications to hydrothermal ore deposits. *Rev. Miner. Geochem.* **1984**, *13*, 469–493.
23. Sallet, R. Fluorine as a tool in the petrogenesis of quartz-bearing magmatic associations: Applications of an improved F-OH biotite-apatite thermometer grid. *Lithos* **2000**, *50*, 241–253. [[CrossRef](#)]
24. Ishihara, S. *Major Molybdenum Deposits and Related Granitic Rocks in Japan*; Geological Survey of Japan: Tokyo, Japan, 1971; Volume 239.
25. Nash, W.P. Phosphate minerals in terrestrial igneous and metamorphic rocks. In *Phosphate Minerals*; Nriagu, J., Moore, P., Eds.; Springer: Berlin, Germany, 1984; pp. 215–241.
26. Teiber, H.; Marks, M.A.; Arzamastsev, A.A.; Wenzel, T.; Markl, G. Compositional variation in apatite from various host rocks: Clues with regards to source composition and crystallization conditions. *J. Miner. Geochem.* **2015**, *192*, 151–167. [[CrossRef](#)]
27. Ishihara, S.; Moriyama, T. Apatite Composition of Representative Magnetite-series and Ilmenite-series Granitoids in Japan. *Resour. Geol.* **2016**, *66*, 55–62. [[CrossRef](#)]
28. Sha, L.-K.; Chappell, B.W. Apatite chemical composition, determined by electron microprobe and laser-ablation inductively coupled plasma mass spectrometry, as a probe into granite petrogenesis. *Geochim. Cosmochim. Acta* **1999**, *63*, 3861–3881. [[CrossRef](#)]
29. Chu, M.-F.; Wang, K.-L.; Griffin, W.L.; Chung, S.-L.; O'Reilly, S.Y.; Pearson, N.J.; Iizuka, Y. Apatite composition: Tracing petrogenetic processes in Transhimalayan granitoids. *J. Petrol.* **2009**, *50*, 1829–1855. [[CrossRef](#)]
30. Ding, T.; Ma, D.; Lu, J.; Zhang, R. Apatite in granitoids related to polymetallic mineral deposits in southeastern Hunan Province, Shi-Hang zone, China: Implications for petrogenesis and metallogenesis. *Ore Geol. Rev.* **2015**, *69*, 104–117. [[CrossRef](#)]
31. Zirner, A.L.; Marks, M.A.; Wenzel, T.; Jacob, D.E.; Markl, G. Rare Earth Elements in apatite as a monitor of magmatic and metasomatic processes: The Ilímaussaq complex, South Greenland. *Lithos* **2015**, *228*, 12–22. [[CrossRef](#)]

32. Broom-Fendley, S.; Styles, M.T.; Appleton, J.D.; Gunn, G.; Wall, F. Evidence for dissolution-precipitation of apatite and preferential LREE mobility in carbonatite-derived late-stage hydrothermal processes. *Am. Miner.* **2016**, *101*, 596–611. [[CrossRef](#)]
33. Roegge, J.S.; Logsdon, M.J.; Young, H.S.; Barr, H.B.; Borcsik, M.; Holland, H.D. Halogens in apatites from the Providencia area, Mexico. *Econ. Geol.* **1974**, *69*, 229–240. [[CrossRef](#)]
34. Williams, S.A.; Cesbron, F.P. Rutile and apatite: Useful prospecting guides for porphyry copper deposits. *Miner. Mag.* **1977**, *41*, 288–292. [[CrossRef](#)]
35. Belousova, E.A.; Walters, S.; Griffin, W.L.; O'Reilly, S.Y. Trace-element signatures of apatites in granitoids from the Mt Isa Inlier, northwestern Queensland. *Aust. J. Earth Sci.* **2001**, *48*, 603–619. [[CrossRef](#)]
36. Belousova, E.A.; Griffin, W.L.; O'Reilly, S.Y.; Fisher, N.I. Apatite as an indicator mineral for mineral exploration: Trace-element compositions and their relationship to host rock type. *J. Geochem. Explor.* **2002**, *76*, 45–69. [[CrossRef](#)]
37. Imai, A. Metallogenesis of Porphyry Cu Deposits of the Western Luzon Arc, Philippines: K-Ar ages, SO₃ Contents of Microphenocrystic Apatite and Significance of Intrusive Rocks. *Resour. Geol.* **2002**, *52*, 147–161. [[CrossRef](#)]
38. Imai, A. Variation of Cl and SO₃ contents of microphenocrystic apatite in intermediate to silicic igneous rocks of Cenozoic Japanese island arcs: Implications for porphyry Cu metallogenesis in the Western Pacific Island arcs. *Resour. Geol.* **2004**, *54*, 357–372. [[CrossRef](#)]
39. Boswell, J.T. *Porphyry System Fertility Discrimination and Mineralization Vectoring Using Igneous Apatite Substitutions to Derive Pre-Exsolution Melt Mineralization Component Concentrations*; The University of Utah: Salt Lake City, UT, USA, 2014.
40. Mao, M.; Rukhlov, A.S.; Rowins, S.M.; Spence, J.; Coogan, L.A. Apatite trace element compositions: A robust new tool for mineral exploration. *Econ. Geol.* **2016**, *111*, 1187–1222. [[CrossRef](#)]
41. Duan, D.-F.; Jiang, S.-Y. Using apatite to discriminate synchronous ore-associated and barren granitic rocks: A case study from the Edong metallogenic district, South China. *Lithos* **2018**, *310*, 369–380. [[CrossRef](#)]
42. Whalen, J.B. *Geology, Petrography, and Geochemistry of Appalachian Granites in New Brunswick and Gaspésie, Quebec*; Geological Survey of Canada: Ottawa, ON, Canada, 1993; Volume 436.
43. Azadbakht, Z.; McFarlane, C.E.; Lentz, D.R. Precise U-Pb ages for the cogenetic alkaline Mount LaTour and peraluminous Mount Elizabeth granites of the South Nepisiguit River Plutonic Suite, northern New Brunswick, Canada. *Atl. Geol.* **2016**, *52*, 189–210. [[CrossRef](#)]
44. Wilson, R.A.; Kamo, S.L. Geochronology and litho-geochemistry of granitoid rocks from the central part of the Central plutonic belt, New Brunswick, Canada: Implications for Sn-W-Mo exploration. *Atl. Geol.* **2016**, *52*, 125–167. [[CrossRef](#)]
45. Whalen, J.B.; Jenner, G.A.; Hegner, E.; Gariépy, C.; Longstaffe, F.J. Geochemical and isotopic (Nd, O, and Pb) constraints on granite sources in the Humber and Dunnage zones, Gaspésie, Quebec, and New Brunswick: Implications for tectonics and crustal structure. *Can. J. Earth Sci.* **1994**, *31*, 323–340. [[CrossRef](#)]
46. Whitney, D.L.; Evans, B.W. Abbreviations for names of rock-forming minerals. *Am. Miner.* **2010**, *95*, 185–187. [[CrossRef](#)]
47. Walker, J.; Gower, S.; McCutcheon, S. Antinouri-Nicholas Project, Gloucester and Restigouche Counties, Northern New Brunswick. In *Sixteenth Annual Review of Activities*; Abbon, S., Ed.; Mineral and Energy Division, Department of Natural Resources and Energy: Fredericton, NB, Canada, 1991; pp. 87–100.
48. Shinkle, D.A. The Long Lake Uranium Prospect: Intragranitic Vein-Type Uranium Mineralization in North-central New Brunswick, Canada. Ph.D. Thesis, University of New Brunswick, Saint John, NB, Canada, 2011.
49. MacLellan, H.E. *Geology and Geochemistry of Middle Devonian Burnthill Brook Granites and Related Tin-Tungsten Deposits, York and Northumberland Counties, New Brunswick*; Minerals and Energy Division Department of Natural Resources and Energy: Brisbane, Australia, 1990.
50. Bevier, M.L.; Whalen, J.B. U-Pb geochronology of Silurian granites, Miramichi Terrane, New Brunswick¹. *Geol. Surv. Can. Pap.* **1990**, *89*, 93–100.
51. Beal, K.-L.; Lentz, D.R.; Hall, D.C.; Dunning, G. Mineralogical, geochronological, and geochemical characterization of Early Devonian aquamarine-bearing dykes of the Zealand Station beryl and molybdenite deposit, west central New Brunswick. *Can. J. Earth Sci.* **2010**, *47*, 859–874. [[CrossRef](#)]

52. Yang, X.-M.; Lentz, D.R.; Chi, G.; Kyser, T.K. Fluid-mineral reaction in the Lake George Granodiorite, New Brunswick, Canada: Implications for Au-W-Mo-Sb mineralization. *Can. Miner.* **2004**, *42*, 1443–1464. [[CrossRef](#)]
53. White, T. The Early Devonian, Evandale Porphyry Cu-Mo-(Au) Deposit, Southern New Brunswick: Petrologic, Geochemical, Geothermobarometric, and Geochronologic Characterization of the Host Rocks and Its Origin. Ph.D. Thesis, University of New Brunswick, Fredericton, NB, Canada, 2013.
54. Mohammadi, N.; Fyffe, L.; McFarlane, C.R.; Thorne, K.G.; Lentz, D.R.; Charnley, B.; Branscombe, L.; Butler, S. Geological relationships and laser ablation ICP-MS U-Pb geochronology of the Saint George Batholith, southwestern New Brunswick, Canada: Implications for its tectonomagmatic evolution. *Atl. Geol.* **2017**, *53*, 207–240. [[CrossRef](#)]
55. Fyffe, L.R.; Richard, D. *Lithological Map of New Brunswick*; Map Plate 2007-18; Mineral and Energy Division, Department of Natural Resources and Energy: Fredericton, NB, Canada, 2007.
56. Whalen, J.B.; Fyffe, L.R.; Longstaffe, F.J.; Jenner, G.A. The position and nature of the Gander-Avalon boundary, southern New Brunswick, based on geochemical and isotopic data from granitoid rocks. *Can. J. Earth Sci.* **1996**, *33*, 129–139. [[CrossRef](#)]
57. Whalen, J.B.; Jenner, G.A.; Longstaffe, F.J.; Hegner, E. Nature and evolution of the eastern margin of Iapetus: Geochemical and isotopic constraints from Siluro-Devonian granitoid plutons in the New Brunswick Appalachians. *Can. J. Earth Sci.* **1996**, *33*, 140–155. [[CrossRef](#)]
58. Whalen, J.B.; Jenner, G.A.; Currie, K.L.; Barr, S.M.; Longstaffe, F.J.; Hegner, E. Geochemical and isotopic characteristics of granitoids of the Avalon Zone, southern New Brunswick: Possible evidence for repeated delamination events. *J. Geol.* **1994**, *102*, 269–282. [[CrossRef](#)]
59. Van Staal, C.R.; Whalen, J.B.; Valverde-Vaquero, P.; Zagorevski, A.; Rogers, N. Pre-Carboniferous, episodic accretion-related, orogenesis along the Laurentian margin of the northern Appalachians. *Geol. Soc. Lond. Spec. Publ.* **2009**, *327*, 271–316. [[CrossRef](#)]
60. Yang, X.-M.; Lentz, D.R.; Chi, G.; Thorne, K.G. Geochemical characteristics of gold-related granitoids in southwestern New Brunswick, Canada. *Lithos* **2008**, *104*, 355–377. [[CrossRef](#)]
61. New Brunswick Bedrock Lexicon. Available online: http://dnr-mrn.gnb.ca/Lexicon/Lexicon/Lexicon_Search.aspx (accessed on 21 October 2018).
62. Mineral Occurrence Database. Available online: <http://dnre-mrne.gnb.ca/mineraloccurrence> (accessed on 21 October 2018).
63. Yang, X.-M. Estimation of crystallization pressure of granite intrusions. *Lithos* **2017**, *286*, 324–329. [[CrossRef](#)]
64. McLeod, M.J.; Taylor, R.P.; Lux, D.R. Geology, Ar/Ar geochronology and Sn-W-Mo-bearing sheeted veins of the Mount Douglas Granite, southwestern New Brunswick. *Can. Inst. Min. Metall. Bull.* **1988**, *81*, 70–77.
65. Bevier, M.L. U-Pb geochronologic studies of igneous rocks in NB. In *Thirteenth Annual Review of Activities, Project Résumés: New Brunswick Department of Natural Resources and Energy, Minerals and Energy Division, Information Circular*; New Brunswick Department of Natural Resources and Energy, Minerals and Energy Division: Ottawa, ON, Canada, 1988.
66. McLeod, M.J. *Geology, Geochemistry, and Related Mineral Deposits of the Saint George Batholith, Charlotte, Queens, and Kings Counties, New Brunswick*; New Brunswick, Natural Resources and Energy, Mineral Resources: Fredericton, NB, Canada, 1990; Volume 5.
67. Bevier, M.L.; Barr, S.M. U-Pb age constraints on the stratigraphy and tectonic history of the Avalon Terrane, New Brunswick, Canada. *J. Geol.* **1990**, *98*, 53–63. [[CrossRef](#)]
68. Thorne, K.G.; Lentz, D.R.; Hall, D.C.; Yang, X. *Petrology, Geochemistry, and Geochronology of the Granitic Pegmatite and Aplite Dykes Associated with the Clarence Stream Gold Deposit, Southwestern New Brunswick*; Natural Resources Canada, Geological Survey of Canada: Ottawa, ON, Canada, 2002.
69. Smith, E.; Fyffe, L.R. *Bedrock Geology of the Hayesville Area (NTS 21 J/10)*; Map Plate MP 2006-1; Carleton, York, and Northumberland Counties: Fredericton, NB, Canada, 2006.
70. Butt, K.A. Genesis of Granitic Stocks in Southwestern New Brunswick. Ph.D. Thesis, University of New Brunswick, Fredericton, NB, Canada, 1976.
71. Yang, X.; Chi, G.; Lentz, D.R. *Petrochemistry of Lake George Granodiorite Stock and Related Gold Mineralization, York County, New Brunswick*; Natural Resources Canada, Geological Survey of Canada: Ottawa, ON, Canada, 2002.

72. Yang, X.-M.; Hall, D.C.; Chi, G.; Lentz, D.R. *Petrology of the Lake George Granodiorite Stock, New Brunswick: Implications for Crystallization Conditions, Volatile Exsolution, and W-Mo-Au-Sb Mineralization*; Natural Resources Canada, Geological Survey of Canada: Ottawa, ON, Canada, 2002.
73. Jochum, K.P.; Weis, U.; Stoll, B.; Kuzmin, D.; Yang, Q.; Raczek, I.; Jacob, D.E.; Stracke, A.; Birbaum, K.; Frick, D.; et al. Determination of forty two major and trace elements in USGS and NIST SRM glasses by laser ablation-inductively coupled plasma-mass spectrometry. *Geostand. Newsl.* **2011**, *35*, 397–429. [[CrossRef](#)]
74. Wyllie, P.J.; Cox, K.G.; Biggar, G.M. The habit of apatite in synthetic systems and igneous rocks. *J. Petrol.* **1962**, *3*, 238–243. [[CrossRef](#)]
75. Putnis, A. Mineral replacement reactions. *Rev. Miner. Geochem.* **2009**, *70*, 87–124. [[CrossRef](#)]
76. Harlov, D.E. Formation of monazite and xenotime inclusions in fluorapatite megacrysts, Gloserheia Granite Pegmatite, Froland, Bamble Sector, southern Norway. *Miner. Petrol.* **2011**, *102*, 77. [[CrossRef](#)]
77. Harlov, D.E. Apatite: A fingerprint for metasomatic processes. *Elements* **2015**, *11*, 171–176. [[CrossRef](#)]
78. Sun, S.-S.; McDonough, W. Chemical and isotopic systematics of oceanic basalts: Implications for mantle composition and processes. *Geol. Soc. Lond. Spec. Publ.* **1989**, *42*, 313–345. [[CrossRef](#)]
79. Blevin, P.L.; Chappell, B.W. The role of magma sources, oxidation states and fractionation in determining the granite metallogeny of eastern Australia. *Geol. Soc. Am. Spec. Pap.* **1992**, *272*, 305–316.
80. Robb, L. *Introduction to Ore-Forming Processes*; Blackwell Publishing: Oxford, UK, 2005.
81. Li, Z.; Duan, D.; Jiang, S.; Ma, Y.; Yuan, H. In situ Analysis of Major Elements, Trace Elements and Sr Isotopic Compositions of Apatite from the Granite in the Chengchao Skarn-Type Fe Deposit, Edong Ore District: Implications for Petrogenesis and Mineralization. *J. Earth Sci.* **2018**, *29*, 295–306. [[CrossRef](#)]
82. Casillas, R.; Nagy, G.; Panto, G.; Brandle, J.; Forizs, I. Occurrence of Th, U, Y, Zr, and REE-bearing accessory minerals in late-Variscan granitic rocks from the Sierra de Guadarrama (Spain). *Eur. J. Miner.* **1995**, *7*, 989–1006. [[CrossRef](#)]
83. Bea, F.; Pereira, M.D.; Stroh, A. Mineral/leucosome trace-element partitioning in a peraluminous migmatite (a laser ablation-ICP-MS study). *Chem. Geol.* **1994**, *117*, 291–312. [[CrossRef](#)]
84. Fujimaki, H. Partition coefficients of Hf, Zr, and REE between zircon, apatite, and liquid. *Contrib. Miner. Petrol.* **1986**, *94*, 42–45. [[CrossRef](#)]
85. Rollinson, H.R. *Using Geochemical Data: Evaluation, Presentation, Interpretation*; Longman: London, UK, 1993.
86. Montel, J.-M. A model for monazite/melt equilibrium and application to the generation of granitic magmas. *Chem. Geol.* **1993**, *110*, 127–146. [[CrossRef](#)]
87. Webster, J.D.; Tappen, C.M.; Mandeville, C.W. Partitioning behavior of chlorine and fluorine in the system apatite–melt–fluid. II: Felsic silicate systems at 200 MPa. *Geochim. Cosmochim. Acta* **2009**, *73*, 559–581. [[CrossRef](#)]
88. Lassiter, J.C.; Hauri, E.H.; Nikogosian, I.K.; Barszczus, H.G. Chlorine-potassium variations in melt inclusions from Raivavae and Rapa, Austral Islands: Constraints on chlorine recycling in the mantle and evidence for brine-induced melting of oceanic crust. *Earth Planet. Sci. Lett.* **2002**, *202*, 525–540. [[CrossRef](#)]
89. Stroncik, N.A.; Haase, K.M. Chlorine in oceanic intraplate basalts: Constraints on mantle sources and recycling processes. *Geology* **2004**, *32*, 945–948. [[CrossRef](#)]
90. Blevin, P.L.; Chappell, B.W. Chemistry, origin, and evolution of mineralized granites in the Lachlan fold belt, Australia; the metallogeny of I- and S-type granites. *Econ. Geol.* **1995**, *90*, 1604–1619. [[CrossRef](#)]
91. Candela, P.A.; Holland, H.D. The partitioning of copper and molybdenum between silicate melts and aqueous fluids. *Geochim. Cosmochim. Acta* **1984**, *48*, 373–380. [[CrossRef](#)]
92. Eugster, H.P. Granites and hydrothermal ore deposits: A geochemical framework. *Miner. Mag.* **1985**, *49*, 7–23. [[CrossRef](#)]
93. Vigneresse, J.-L. The role of discontinuous magma inputs in felsic magma and ore generation. *Ore Geol. Rev.* **2007**, *30*, 181–216. [[CrossRef](#)]
94. Lalonde, A.; Bernard, P. Composition and color of biotite from granites: Two useful properties in the characterization of plutonic suites from the Hefburn internal zone of Wopmay Orogen, Northwest Territories. *Can. Miner.* **1993**, *31*, 203–217.
95. Ishihara, S. The granitoid series and mineralization. *Econ. Geol.* **1981**, *75*, 458–484.
96. Watson, E.B.; Green, T.H. Apatite/liquid partition coefficients for the rare earth elements and strontium. *Earth Planet. Sci. Lett.* **1981**, *56*, 405–421. [[CrossRef](#)]

97. Dawson, J.B.; Hinton, R.W. Trace-element content and partitioning in calcite, dolomite and apatite in carbonatite, Phalaborwa, South Africa. *Miner. Mag.* **2003**, *67*, 921–930. [[CrossRef](#)]
98. Klemme, S.; Dalpé, C. Trace-element partitioning between apatite and carbonatite melt. *Am. Miner.* **2003**, *88*, 639–646. [[CrossRef](#)]
99. Turner, S.; Foden, J.U. Th and Ra disequilibria, Sr, Nd and Pb isotope and trace element variations in Sunda arc lavas: Predominance of a subducted sediment component. *Contrib. Miner. Petrol.* **2001**, *142*, 43–57. [[CrossRef](#)]
100. Labanieh, S.; Chauvel, C.; Germa, A.; Quidelleur, X. Martinique: A clear case for sediment melting and slab dehydration as a function of distance to the trench. *J. Petrol.* **2012**, *53*, 2441–2464. [[CrossRef](#)]
101. Blevin, P.L. Redox and Compositional Parameters for Interpreting the Granitoid Metallogeny of Eastern Australia: Implications for Gold-rich Ore Systems. *Resour. Geol.* **2004**, *54*, 241–252. [[CrossRef](#)]
102. Exley, R.A. Microprobe studies of REE-rich accessory minerals: Implications for Skye granite petrogenesis and REE mobility in hydrothermal systems. *Earth Planet. Sci. Lett.* **1980**, *48*, 97–110. [[CrossRef](#)]



© 2018 by the authors. Licensee MDPI, Basel, Switzerland. This article is an open access article distributed under the terms and conditions of the Creative Commons Attribution (CC BY) license (<http://creativecommons.org/licenses/by/4.0/>).